HOCHSCHULE LANDSHUT
HOCHSCHULE FÜR ANGEWANDTE WISSENSCHAFTEN

FAKULTÄT ELEKTROTECHNIK &
WIRTSCHAFTSINGENIEURWESEN

Masterarbeit

Sensitivity Analysis of Model-based Pol-TomoSAR Decomposition for Ground-Volume Separation and Soil Moisture Retrieval over Agricultural Areas

Klemens Reberger

Prüferin: Prof. Hannah Jörg
Betreuer: Prof. Irena Hajnsek, Nikita Basargin

ERKLÄRUNG ZUR MASTERARBEIT

Reberger, Klemens

Hochschule Landshut
Fakultät Elektrotechnik & Wirtschaftsingenieurwesen

Hiermit erkläre ich, dass ich die Arbeit selbständig verfasst, noch nicht anderweitig für Prüfungszwecke vorgelegt, keine anderen als die angegebenen Quellen oder Hilfsmittel benützt, sowie wörtliche und sinngemäße Zitate als solche gekennzeichnet habe.

....	....
(Datum)	(Unterschrift des Studierenden)

FREIGABEERKLÄRUNG DER/DES STUDENT(IN)EN

Name, Vorname der/des Student(in)en:

Reberger, Klemens

Hiermit erkläre ich, dass die vorliegende Masterarbeit in den Bestand der Hochschulbibliothek aufgenommen werden kann und

- ☐ ohne Sperrfrist

oder nach einer Sperrfrist von

- ☐ 1 Jahr
- ☐ 2 Jahren
- ☐ 3 Jahren
- ☐ 5 Jahren
- ☐ 10 Jahren oder länger

über die Hochschulbibliothek zugänglich gemacht werden darf.

19.12.2024
(Datum)

(Unterschrift der/des Student(in)en)

Abstract

One method for estimating soil moisture is through the use of radar systems, such as Synthetic Aperture Radar (SAR), due to their high spatial resolution. However, this presents a significant challenge when the soil is situated beneath a vegetative canopy, as the vegetation exerts a considerable influence on the backscattered signal. In order to distinguish between vegetation and the ground, this thesis concentrates on the utilisation of interferometric multi-baseline airborne F-SAR data for the acquisition of vertical information and polarimetric airborne F-SAR data for the estimation of soil moisture. To this end, the problem is initially divided into two sub-problems. The initial issue concerns the separation of the ground and vegetation layers. This entails defining the vertical reflectivity profile of the ground layer and the polarimetric volume signature of the vegetation, as well as calculating the corresponding polarimetry matrix for the ground. This is achieved through optimisation, which enables the imposition of a high degree of variability in additional constraints. The second sub-problem concerns the estimation of soil moisture, employing physical models. This study demonstrates that even when ground and volume separation is acceptable, it is not possible to uniquely calculate soil moisture using physical models. Consequently, we demonstrate that by integrating the physical models directly into the layer separation, the solution aligns with the models but is not unique. By constraining the powers of the components, we are able to estimate soil moisture with sufficient precision. The findings indicate that it is feasible to estimate soil moisture with the imposed constraints, while also highlighting the importance of accurately defining the corresponding power constraints.

Contents

1 Introduction

In light of the ongoing phenomenon of climate change, the importance of environmental monitoring is becoming increasingly evident. In this context, specific focus is being directed towards the domain of agriculture in relation to food security. It is of significant importance to monitor soil moisture, which plays a pivotal role in agricultural practices. The accurate measurement and monitoring of soil moisture on extensive agricultural regions is crucial for the optimisation of watering techniques and the effective administration of water resources. Given its intrinsic characteristics and the growing number of space-based Synthetic Aperture Radar (SAR) [1] systems, SAR technology is emerging as a promising tool for monitoring the Earth's surface. Given the often labor-intensive nature of conventional ground soil moisture measurement techniques, there is an opportunity to determine this using SAR data, particularly given the high resolution.

It has been demonstrated that soil moisture can be determined through the use of polarimetric data (PolSAR) acquired through SAR. For example, the potential for utilising PolSAR data in agricultural areas without vegetation has already been investigated [2]. The calculation of soil moisture under vegetation is a considerably more challenging undertaking, due to the considerable influence that vegetation exerts on the signal, and therefore on the accuracy of the results [3]. As PolSAR data represent backscattered signals of an environment, the accuracy of the results can be enhanced by separating the signal into ground and vegetation layers. The separation of ground and volume layers is possible with multi-baseline SAR data (TomoSAR) [4].

One potential solution for the separation of ground and volume layers is the utilisation of polarimetric and multi-baseline information data (Pol-TomoSAR) with the Sum of Kronecker Products (SKP) decomposition [5], which has been evaluated for forest areas. In this approach, the scattering contributions are separated according to their vertical profile and polarimetric scattering mechanisms. The original formulation of the SKP decomposition does not impose constraints and does not integrate physical models into the calculation, which would facilitate a more straightforward interpretation. Additionally, the solutions derived from this method may not always be physically interpretable. One potential solution to this issue is to define the SKP decomposition as an optimisation problem that can be readily adapted to incorporate additional constraints. This optimisation problem can then be solved using the numerical optimisation method backpropagation [6], which has been successfully employed for constrained tensor decomposition for SAR data [7].

The issue is addressed from two distinct perspectives. The soil moisture estimation problem is initially divided into two distinct steps. The preliminary phase involves the separation of the ground and vegetation layers using a customised SKP decomposition. Subsequently, the ground layer is utilised in an attempt to calculate soil moisture through the application of physical models, with the inherent limitations of such an approach being shown. The second approach seeks to address the shortcomings of the first by integrating physical models into the optimisation process. This integration enables the simultaneous determination of ground and vegetation separation and soil moisture estimation.

The data obtained from the CROPEX14 campaign is employed for the purpose of evaluating the various methods utilized. This is a comprehensive polarimetric multi-baseline airborne dataset of agricultural regions at X/C/L-Band of Wallerfing test site in southern Germany, acquired between May and August 2014. For the purposes of this study, we limit our analysis to a maize field and the L-Band frequency. The maize field was selected to demonstrate performance of the algorithm in presence of high vegetation and the L-band's ability to penetrate deeper into the vegetation, resulting in enhanced signal from the ground.

This thesis aims to address the following scientific questions in detail:

- How sensitive is the estimation of soil moisture using the H/α space (Section 2.1.1) of physical models with the ground polarimetry matrix resulting from constrained two-step SKP decomposition?
- How can the soil moisture estimation be improved by integrating the physical models into a single step SKP decomposition?

- What is the effect of the parameters of the physical models on the cost function with respect to soil moisture?

In order to answer these questions, it is first necessary to present a brief overview of the fundamental principles underlying the application of SAR techniques. The following section examines the SKP decomposition and the backpropagation procedure, which is employed to resolve the presented SKP. Subsequently, the data under investigation are presented, and the two-step decomposition is tested on them. This process begins with the separation of ground and vegetation, followed by the determination of soil moisture from the ground component using the H/α space of the physical models. Thereafter, the one-step decomposition is examined, whereby the physical models are integrated into the SKP decomposition. Finally, the two methods are compared and the results are discussed.

2 Synthetic Aperture Radar

Synthetic Aperture Radar (SAR) [1] is an active remote sensing radar system that works like a conventional radar by measuring the backscattered portion of sequentially transmitted electromagnetic waves, except that it uses the movement of the antenna. Through the movement of the transmitter, it is possible to create a simulated/virtual antenna that is much longer than the physical one, which allows a higher azimuth resolution of the 2D images compared to a static radar. The resolution in the range direction is identical to that of static radar, depending only on the bandwidth of the transmitted signal. The enhanced resolution in the azimuth direction can be attributed to the synthetic aperture, which is determined by multiplying the beam width of the antenna by the slant range. By simplifying the aforementioned terms, it becomes evident that the azimuth resolution is solely determined by the length of the antenna. The whole SAR imaging geometry can be seen in Fig. 2.1.

The received signal is then stored in a matrix where each pixel represents the complex value of the signal backscattered to the antenna. The amplitude describes the

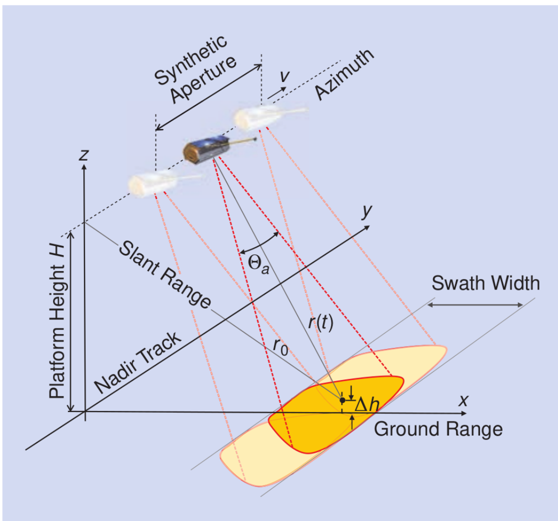

Figure 2.1: SAR imaging geometry [1].

strength of the backscattered signal and the phase describes time the signal needed to come back (phase difference). In order to obtain a SAR image, the raw data must must be preprocessed using digital filters.

One of the distinctive characteristics of SAR images is the phenomenon of speckle, which arises from the random distribution of scatterers and presents as granular noise. A resolution cell of the SAR image is interpreted as the coherent sum of the received signals from all scatterers. Therefore, even small geometric changes in the scene with the same scatterers can affect the received signal. This is attributable to the differing phases of the signals back scattered by the various scatterers, which interact with one another and thus exert an influence on the overall sum. This can have a large effect, as two almost identical neighbouring pixels can have about the same scatterers, but look very different in the image, as shown in Fig. 2.2. To reduce the effect of speckle, the data is averaged over a given window, a technique called multi-looking, which is calculated using a spatial filter .
Basic SAR only measures the back scattered signal of a specific polarisation. An extension of SAR is SAR polarimetry, where data from different polarisations are considered for analysis. This provides additional physical information as different scatterers react differently to each polarisation, providing additional ways to

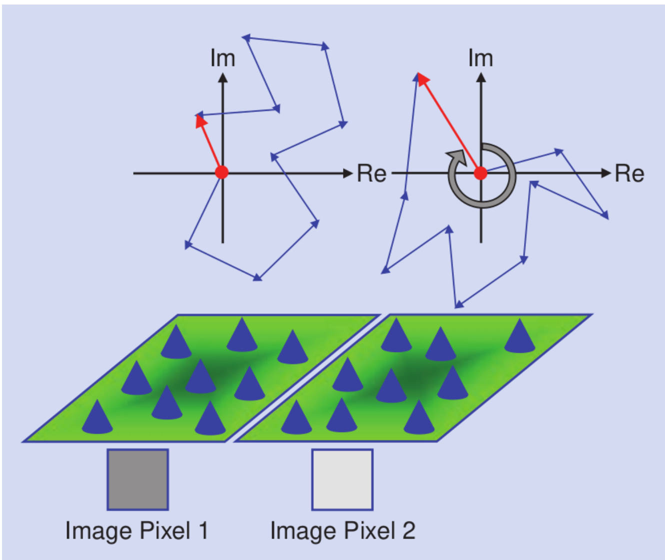

Figure 2.2: The effect of speckle on two neighbouring resolution cells with the same amount of scatterers is displayed, where the coherent sum is shown to be different [1].

interpret the data.

2.1 SAR Polarimetry

SAR Polarimetry [8] is a technique for evaluating qualitative and quantitative physical information by measuring polarimetric properties of scatterers. To do this, two orthogonally polarized signals (wave vectors $\mathbf{e}_H = \begin{pmatrix} 1 \\ 0 \end{pmatrix}$ and $\mathbf{e}_V = \begin{pmatrix} 0 \\ 1 \end{pmatrix}$ with $\mathbf{e} \in \mathbb{C}^2$) are sent and the backscattering is received. These values are stored in a $\mathbf{S} \in \mathbb{C}^{2\times 2}$ scattering matrix (in the monostatic case also known as Sinclair matrix) that describes the transformation of the transmitted signal by the scatterer and is given by:

$$\mathbf{S} = \begin{pmatrix} S_{HH} & S_{HV} \\ S_{VH} & S_{VV} \end{pmatrix} = e^{i\phi_{VV}} \begin{pmatrix} |S_{HH}| \cdot e^{i(\phi_{HH}-\phi_{VV})} & |S_{HV}| \cdot e^{i(\phi_{HV}-\phi_{VV})} \\ |S_{VH}| \cdot e^{i(\phi_{VH}-\phi_{VV})} & |S_{VV}| \end{pmatrix} \tag{2.1}$$

In the monostatic case the scattering matrix becomes symmetric ($S_{HV} = S_{VH}$) for all reciprocal media. The common way to describe $\mathbf{S}$ is as a scattering vector under the Pauli basis

$$\mathbf{k} = \frac{1}{\sqrt{2}}(S_{HH} + S_{VV}, S_{HH} - S_{VV}, S_{HV} + S_{VH})^T \tag{2.2}$$

with $\mathbf{k} \in \mathbb{C}^3$ for easier interpretation of the scattering processes as shown in Fig. 2.3. The following scattering processes can be distinguished:

- $|S_{HH} + S_{VV}|$ can be interpreted as surface scattering for example caused by bare soil or rough water.
- $|S_{HH} - S_{VV}|$ can be interpreted as dihedral scattering (double bounce) for example caused by buildings and tree trunks.
- $|S_{HV} + S_{VH}|$ can be interpreted as random (volume) scattering for example caused by the leaves and canopy of vegetation like tree and maize.

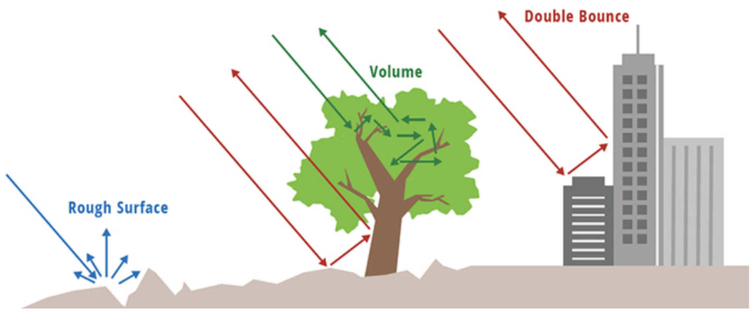

Figure 2.3: Examples of the three scattering mechanisms [9].

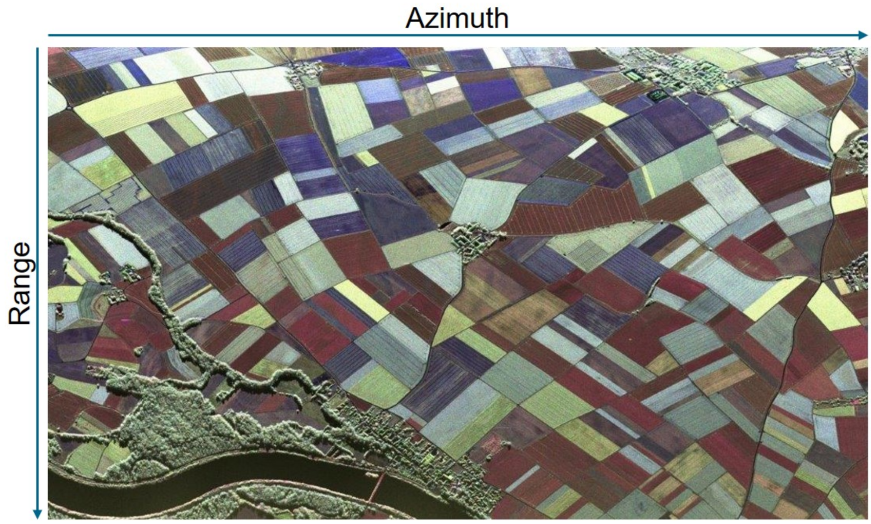

Figure 2.4: The Pauli RGB example of the Wallerfing test site from 04.06.2014 at C-Band illustrates scattering mechanisms with different colours $|S_{HH}+S_{VV}|$ in blue, $|S_{HH}-S_{VV}|$ in red, and $|S_{HV}-S_{VH}|$ in green.

The Pauli vector can also be used to visualise the scattering process in a Pauli RGB image like Fig. 2.4 for easier interpretation.
The defined scattering could describe deterministic scatterers, but fails to describe the distributed scatterers. To gain more information of the scattering mechanism a second order statistic is needed. This is achieved by defining the coherency matrix $\mathbf{T} \in \mathbb{C}^{3\times 3}$ as the outer product of the Pauli vector $\mathbf{k}$ with the Hermitian transpose of itself and averaged over l neighbouring pixels for multi-looking

$$\mathbf{T} = \frac{1}{l}\sum_{j=1}^{l} \mathbf{k}_j \mathbf{k}_j^H. \tag{2.3}$$

The selection of the multi-look window size represents a compromise between spatial resolution and speckle reduction and has the effect that the coherency matrix $\mathbf{T}$

is full rank [8].
The main purpose of calculating the coherency matrix is to decompose it into different scattering mechanisms within the resolution cell and to extract physical information such as soil moisture. The following section examines a number of established methods for decomposing the coherency matrix.

2.1.1 Eigenvalue decomposition

The eigenvalue decomposition (EVD) [10] is briefly presented next. Using the EVD, it is possible to decompose the coherency matrix as follows:

$$\mathbf{T} = \mathbf{U}\Lambda\mathbf{U}^{-1} \tag{2.4}$$

with $\mathbf{U} \in \mathbb{C}^{3\times3}$ as the matrix with the eigenvectors and $\Lambda \in \mathbb{R}^{3\times3}$ as the matrix with the corresponding eigenvalues on the diagonal. Since the coherency matrix is Hermitian, the eigenvectors are orthonormal. The eigenvectors $\mathbf{e}_j$ could be further described as:

$$\mathbf{e}_j = \begin{pmatrix} \cos(\alpha_j)e^{i\phi_{1j}} \\ \sin(\alpha_j)\cos(\beta_j)e^{i\phi_{2j}} \\ \sin(\alpha_j)\sin(\beta_j)e^{i\phi_{3j}} \end{pmatrix} \tag{2.5}$$

for further determination of the scattering mechanism. The alpha angle α_j can be used to associate the eigenvector with a scattering process and the beta angle with the line-of-sight rotation. Often, the weighted average of all alphas of the eigenvectors ($\alpha_{mean} = \sum_{j=1}^{3} P_j \cdot \alpha_j$) is used to describe the scattering process of the entire polarimetry matrix.
One of the applications of the EVD is the calculation of the polarimetric scattering entropy as introduced in [8] through the utilisation of eigenvalues.

$$H = -\sum_{i=1}^{3} P_i log_3 P_i \tag{2.6}$$

$$P_i = \frac{\lambda_i}{\lambda_1 + \lambda_2 + \lambda_3} \tag{2.7}$$

which is a general measure of the scattering depolarisation.
It is characterised by the following features:

- $0 \leq H \leq 1$

- $H = 0 \rightarrow$ totally polarised scatterer: $\lambda_2 = \lambda_3 = 0$
- $H = 1 \rightarrow$ totally unpolarised scatterer: $\lambda_1 = \lambda_2 = \lambda_3$

With the two parameters α (from the eigenvector) and H (from the eigenvalues), it is now possible to further classify the scattering mechanisms.
Another derived parameter from the eigenvalues is the scattering anisotropy

$$A = \frac{\lambda_2 - \lambda_3}{\lambda_2 + \lambda_3} \tag{2.8}$$

which provides information about the variation of depolarisation with changing polarisation.
It is characterised by the following features:

- $0 \leq A \leq 1$
- $A = 0 \rightarrow$ depolarisation remains the same across all polarimetric sub-spaces
- $A = 1 \rightarrow$ there are polarimetric subspaces with low(er) depolarisation.

With this approach it is already possible to estimate geophysical parameters such as soil moisture [2]. The estimation is done using a look-up table obtained from physically based models. The subsequent section examines model-based decomposition, whereby the physical-derived formulas of the scattering mechanisms serve as the primary focus.

2.1.2 Model-based decomposition

This section examines data decompositions that solely employ physical models for their description. The objective is to approximate the data using a set of physically defined contributions, for example, those related to surface and volume scattering. One of the first model-based decomposition introduced is the three-component decomposition proposed by A. Freeman and S.L. Durden [11]. This model consists of Bragg (surface), dihedral (double bounce) and volume scattering

$$\mathbf{T} = f_s \begin{pmatrix} 1 & b^* & 0 \\ b & |b|^2 & 0 \\ 0 & 0 & 0 \end{pmatrix} + f_d \begin{pmatrix} |a|^2 & a & 0 \\ a^* & 1 & 0 \\ 0 & 0 & 0 \end{pmatrix} + \frac{f_v}{4} \begin{pmatrix} 2 & 0 & 0 \\ 0 & 1 & 0 \\ 0 & 0 & 1 \end{pmatrix}. \tag{2.9}$$

It can be demonstrated that the parameter b is dependent upon the dielectric constant of the surface and the incidence angle. Moreover, it can be shown that the

parameter a is additionally dependent upon the stem dielectric constant [2].
The following section provides a detailed examination of the physical models associated with the three scattering mechanisms.

X-Bragg model

A basic model for surface scattering is the Bragg model [8]. One parameter on which it depends on are the horizontal Bragg coefficient

$$R_v = \frac{\cos\theta - \sqrt{\varepsilon_s - \sin^2\theta}}{\cos\theta + \sqrt{\varepsilon_s - \sin^2\theta}} \tag{2.10}$$

and the vertical Bragg coefficient

$$R_v = \frac{(\varepsilon_s - 1)(\sin^2\theta - \varepsilon_s(1 + \sin^2\theta))}{(\varepsilon_s\cos\theta + \sqrt{\varepsilon_s - \sin^2\theta})^2}, \tag{2.11}$$

with θ as the incidence angle and ε_s as the dielectric constant of soil. Another parameter is the scattering power $f_s = \frac{m_s^2}{\sqrt{2}}|R_h + R_v|^2$ and with the ratio $\beta = \frac{R_h - R_v}{R_h + R_v}$ the Bragg coherency matrix can be represented as follows:

$$\mathbf{T}_{Bragg} = f_S \begin{pmatrix} 1 & \beta^* & 0 \\ \beta & |\beta|^2 & 0 \\ 0 & 0 & 0 \end{pmatrix}. \tag{2.12}$$

To expand the scope of the Bragg model and incorporate cross-polarised scattering and depolarisation effects, the X-Bragg model was introduced in [2]. This results in the coherency matrix

$$\mathbf{T}_{X-Bragg} = f_s \begin{pmatrix} 1 & \beta^* sinc(2\delta) & 0 \\ \beta sinc(2\delta) & \frac{1}{2}|\beta|^2(1 + sinc(4\delta)) & 0 \\ 0 & 0 & \frac{1}{2}|\beta|^2(1 + sinc(4\delta)) \end{pmatrix}, \tag{2.13}$$

with δ as the parameter for the depolarization. In the specific instance where $\delta = 0$, the coherency matrices are identical, namely $\mathbf{T}_{Bragg} = \mathbf{T}_{X-Bragg}$.

Dihedral model

The following section examines the physical model of the dihedral scattering mechanism, which is caused by the double reflection of soil and vegetation (stem) .A basic model [8] can be described by the horizontal Fresnel coefficient

$$R_{ih} = \frac{\cos\theta_i - \sqrt{\varepsilon_i - \sin^2\theta_i}}{\cos\theta_i + \sqrt{\varepsilon_i - \sin^2\theta_i}} \tag{2.14}$$

and the vertical Fresnel coefficient

$$R_{iv} = \frac{\varepsilon_i \cos\theta_i - \sqrt{\varepsilon_i - \sin^2\theta_i}}{\varepsilon_i \cos\theta_i + \sqrt{\varepsilon_i - \sin^2\theta_i}}, \tag{2.15}$$

with the index i is used to denote the parameter associated with the soil $i = s$ or stem $i = t$. The incidence angle for the stem is given by $\theta_t = \frac{\pi}{2} - \theta$. The scattering power $f_d = \frac{1}{2}|R_{sh}R_{th} + R_{sv}R_{tv}e^{i\varphi}|^2$ and the ratio $\alpha = \frac{R_{sh}R_{th} - R_{sv}R_{tv}e^{i\varphi}}{R_{sh}R_{th} + R_{sv}R_{tv}e^{i\varphi}}$ yield a coherency matrix for dihedral scattering, which can be expressed as follows:

$$\mathbf{T}_{Dihedral} = f_d \begin{pmatrix} |\alpha|^2 & \alpha & 0 \\ \alpha^* & 1 & 0 \\ 0 & 0 & 0 \end{pmatrix}. \tag{2.16}$$

Finally, the term

$$L_s = e^{(-2k^2\sigma^2\cos^2\theta)}, \tag{2.17}$$

where k is the wavenumber and σ is the standard deviation of the vertical roughness, is incorporated into the parameter f_d to account for the reflection losses associated with soil roughness. This results in the final form $f_d = |L_s|^2 \cdot \frac{1}{2}|R_{sh}R_{th} + R_{sv}R_{tv}e^{i\varphi}|^2$.

Volume model

In order to obtain the volume polarimetry matrix, three different oriented dipole scattering elements are considered [3]. One is the polarimetry matrix for random oriented dipole scatterers.

$$\mathbf{T}_v^{(\text{ran})} = f_v \begin{pmatrix} 2 & 0 & 0 \\ 0 & 1 & 0 \\ 0 & 0 & 1 \end{pmatrix}. \tag{2.18}$$

The second polarimetry matrix is for vertical oriented dipole scatterers

$$\mathbf{T}_v^{(\text{ver})} = f_v \begin{pmatrix} 15 & 5 & 0 \\ 5 & 7 & 0 \\ 0 & 0 & 8 \end{pmatrix}. \tag{2.19}$$

The final polarimetry matrix is for horizontal oriented dipole scatterers

$$\mathbf{T}_v^{(\text{hor})} = f_v \begin{pmatrix} 15 & -5 & 0 \\ -5 & 7 & 0 \\ 0 & 0 & 8 \end{pmatrix}. \tag{2.20}$$

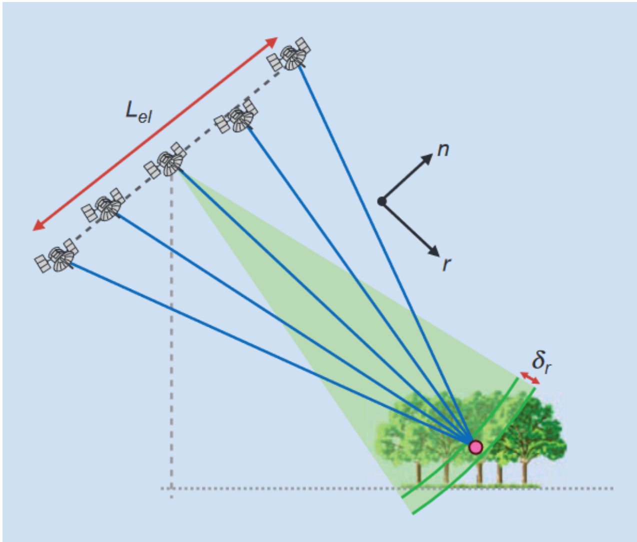

Figure 2.5: SAR tomography acquisition geometry [1]

The aforementioned approaches facilitate the analysis of a resolution cell's signal without the necessity of vertical information. The subsequent method illustrates the retrieval of the vertical distribution of scatterers with the aid of multiple acquisitions of an area that fulfils specific geometric criteria.

2.2 SAR Tomography

SAR tomography [12] represents a technique for the retrieval of vertical information from multiple SAR data sets, utilising the displaced position of the antennas. This method also creates a synthetic aperture, but now in the normal to slant direction, from a set of SAR images acquired at slightly different incidence angles from displaced tracks, as shown in Fig. 2.5. It is standard practice for all SAR images to be of the same polarisation.
A common way to calculate the SAR tomography intensity profile is to use the Fourier algorithm. First we compute the covariance matrix $\mathbf{R} \in \mathbb{C}^{n \times n}$ with n acquisitions. This is done similarly to a coherency matrix in Section 2.1, but instead of Pauli vectors, we use the data vectors $\mathbf{y} = (y_1, y_2, ..., y_n)^T$ with y_i as the SAR signal of the i-th acquisition

$$\mathbf{R} = \frac{1}{n} \sum_{j=1}^{l} \mathbf{y}_j \mathbf{y}_j^H .$$

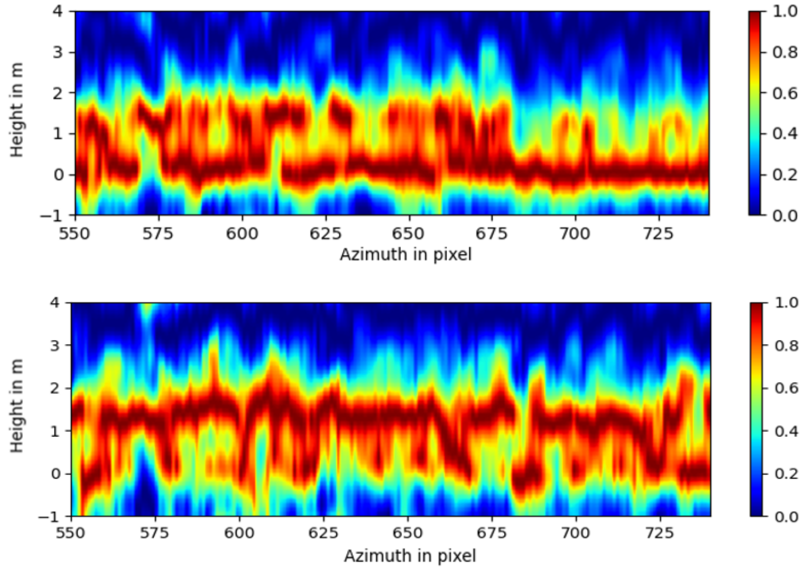

Figure 2.6: Two SAR tomograms of a vegetated maize field at C-Band in HH (top) and VV (bottom) polarisations.

The next step is to calculate the Fourier reference function, which requires the definition of the phase variation of a scattering contribution $\mathbf{a}(z) = (e^{-i\kappa_{z_0}z}, e^{-i\kappa_{z_1}z}, ..., e^{-i\kappa_{z_n}z})^T$, where κ_{z_i} is the vertical wavenumber and z is the given height. The resulting Fourier reference function is then expressed as

$$\mathbf{w}(z) = \frac{1}{n}\mathbf{a}(z). \tag{2.21}$$

At last the vertical reflectivity function $f(z)$ is computed as

$$f(z) = \mathbf{w}(z)^H \cdot \mathbf{R} \cdot \mathbf{w}(z). \tag{2.22}$$

With this method it is possible to calculate a tomogram like in Fig. 2.6.
The SAR tomogram of the maize field, comprising vegetation with a height of 3 m, was acquired over 9 tracks and exhibits a vertical resolution of approximately 1 m. It illustrates the vertical structures, with the ground at zero height and the volume scatterer above. It is evident that the generation of tomograms may vary depending on the selected polarisation. In the HH image, the ground is discernible, while in the VV image, the volume is more prominent, although the surface scattering above the vegetation is also a possibility. It should be noted that, in all tomograms, the reconstructed profiles are normalised to the maximum power at each inversion point.
We have now provided a detailed account of the standard SAR methods that are required to describe the results of the SKP decomposition. This decomposition

process separates the multi-baseline multi-polarimetric data into two distinct components, each of which is comprised of a polarimetric matrix and a structure matrix. The second method is employed for the purpose of calculating the aforementioned SKP decomposition.

3 Methods

This chapter presents two methods. The first method is the SKP decomposition, which allows the ground and vegetation layers to be separated using multi-baseline multi-polarimetric data. For each component, a polarimetry matrix is calculated to describe the scattering mechanisms, and a structure matrix is calculated to describe the corresponding vertical profile. The standard SKP calculation does not allow for a simple integration of constraints; therefore, we consider the decomposition to be an optimisation problem, which we solve using a numerical method that we also present.

3.1 Sum of Kronecker Products decomposition

One introduced method to analyse multi-baseline multi-polarimetric data (MPMB) is the "Sum of Kronecker Products" (SKP) [5]. Here we describe the data matrix $\mathbf{MPMB} \in \mathbb{C}^{3n\times 3n}$, for n tracks, as the sum of Kronecker products. The summands are interpreted as the different scattering mechanisms (SM) contributing to the data covariance matrix. One part of the Kronecker product describes the SM using the polarimetry matrix $\mathbf{T}_i \in \mathbb{C}^{3\times 3}$ and the other part describes its vertical structure $\mathbf{R}_i \in \mathbb{C}^{n\times n}$ of it

$$\mathbf{MPMB} = \sum_{i=1}^{k} \mathbf{R}_i \otimes \mathbf{T}_i, \tag{3.1}$$

where k is interpreted as the amount of different SM.
In order to be able to do this, three assumptions are made:

1. There is no statistically significant correlation between different SM.
2. On every polarimetric channel the interferometric coherences of a specific SM are the same.
3. The polarimetric signature of the SM is the same for all tracks up to a scale factor.

In a few words the decomposition is computed by the Singular Value Decomposition (SVD) [10] of the rearranged data matrix **MPMB**. Subsequently, the matrices $\mathbf{R}_i$ and $\mathbf{T}_i$ are reconstructed from the rows and columns of the resulting unitary matrices **U** and **V**, which are produced by the singular value decomposition (SVD) of the rearranged data matrix **MPMB**.
It is important to highlight that the resulting matrices $\mathbf{R}_i$ and $\mathbf{T}_i$, particularly for $i > 1$, are not always positive semi-definite. This characteristic is of considerable importance, as it is present in the physical models. Consequently, the subsequent stage entails the recombination of the resulting matrices in order to attain the aforementioned property. It is also important to consider that the resulting polarimetry matrices describe a sum of different scattering mechanisms. Therefore, the recombination must also be taken into account, particularly if the separation of scattering mechanisms is of great importance.
Finally, it should be noted that it is not always possible to find a recombination of the matrices which gives positive semi-definite matrices.
A method for decomposing multi-baseline multi-polarimetric data into its constituent components has now been outlined. The following section presents a method for calculating the SKP decomposition, which allows for the attainment of certain additional constraints.

3.2 Optimisation with Backpropagation

Optimisation is a powerful technique that can be used to determine the optimal solution from a set of feasible alternatives. It can be applied to a wide range of problems, including the fitting of data to physical models. The objective of optimisation is to identify the optimal value of the cost function. One common way to compute the optimum of a non-linear function is through iterative gradient-based [13] algorithms, where each iteration should brings us closer to the solution. The direction in which we move is determined by the gradient, which gives the direction of the largest derivative. Therefore, it is necessary to ascertain the gradient of the cost function in advance. It is, of course, possible to compute the gradient directly; however, another approach has gained greater prominence in recent times, due to the growing field of machine learning. This method is known as backpropagation [6]. One significant benefit of this approach is that it facilitates the calculation of the gradient, relying on the operations conducted on the optimisation variables. This is achieved by the construction of a computational graph, which illustrates

the manner in which the parameters are connected to one another through specific operations.
In the first step, called forward pass, all intermediate results to the cost function are calculated from the current values. The next step is called backpropagation, which calculates all the intermediate gradients with the chain rules backwards from the solution of the forward pass. Subsequently, the intermediate optimisation variables are updated in accordance with the gradient [14]. This process is repeated until the solution, which is the cost function, does not change much from the previous iterations (convergence) or a fixed number of iterations.
As previously stated, the method offers a convenient approach to gradient calculation. Furthermore, it is sufficiently adaptable to accommodate modifications, such as the introduction of constraints on variables. However, it should be noted that in general with non-linear problems the optimizer is not guaranteed to find the global minimum. Another disadvantage is that the solution depends strongly on the initial parameters of the algorithm, namely the initial/start values, the step size as well as the termination criterion.
We have thus defined the most important methods that we now apply to the data and present the results.

4 Results

We now proceed to the principal section of the thesis. The following section presents the data that has been analysed to produce the results presented in this thesis. Subsequently, the initial method is presented, namely the two-step decomposition. In the initial phase, the ground and vegetation layers are separated. We commence with an introduction to the method, outlining its constraints, and proceed to analyse the resulting polarimetry matrix for the ground. In the second step, we attempt to ascertain soil moisture values from the resulting polarimetry matrix utilising the H/α space of the X-Bragg and dihedral models.
Subsequently, we examine one-step decomposition, initially delineating the method and subsequently determining soil moisture values with it. We then investigate the dependence of soil moisture estimation on model parameters. Finally, we conduct a comparative analysis of the two methods. We now proceed with the data.

4.1 Data

The following sections presents the CROPEX14 campaign, which was acquired with the F-SAR system [15], as illustrated in Fig. 4.1. This encompasses fully polarimetric multi-baseline airborne data of agricultural regions at X/C/L-Band of Wallerfing, carried out from May to August 2014. The campaign's objective was to study the different phenological stages of a number of crops, including maize. Additionally, soil moisture and height measurements were carried out simultaneously on different days, as detailed in Tab. 4.1.
The subsequent investigations are constrained to the maize field at L-Band (to enhance signal penetration and, consequently, the differentiation of ground and volume) as well as solely the latter flights due to the presence of elevated vegetation. A total of 153 independent looks were obtained by selecting a multi-look window comprising nine looks in range and 17 looks in azimuth direction. This resulted in a resolution of 10m by 10m.
It is also important to consider the uncertainty of the measured soil moisture, as

Figure 4.1: Campaign land use.

illustrated in Fig. 4.2. This figure shows the difference of the measured values in relation to the mean value (6 measurements per position) and the maximum and minimum measured values (per position) for flights 9, 11 and 13.
The Root Mean Square Deviation (RMSD) is a statistical measure that quantifies the deviation between the observed and estimated values. In this context, it is used to assess the deviation between the average measured soil moisture $\mathbf{x}$ and the max/min measured soil moisture values $\mathbf{y}$. The RMSD can be calculated as

$$\mathrm{RMSD} = \frac{||\mathbf{x} - \mathbf{y}||_2}{\sqrt{l}}, \tag{4.1}$$

Flight	Date	Height of maize in m	Average soil moisture in vol%
2	15.05.2014	0.1	22.5
3	22.05.2014	0.1	15.5
6	04.06.2014	0.28	16.5
7	12.06.2014	0.63	10.5
9	18.06.2014	0.9 - 1.05	10.2
11	03.07.2014	1.2 - 1.9	19
13	24.07.2014	2.8 - 3.37	17

Table 4.1: Ground measurements of the big maize field.

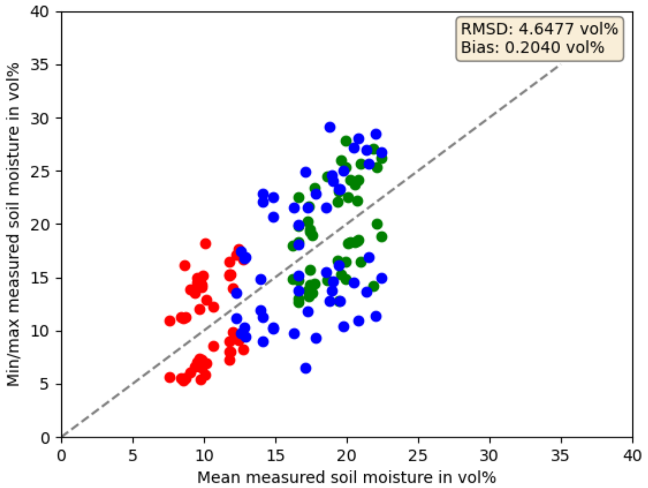

Figure 4.2: Deviation of the measured soil moisture values for flight 9 (red), 11 (green) and 13 (blue)

where l represents the number of measurements and $||.||_2$ the Euclidean norm. The $RMSD = 4.65$ vol% indicates the relative big deviation of the measured values.
The subsequent statistical measure is the bias, which also represents the distinction between the observed and estimated values. This provides an indication of whether there is a general bias in the estimated values, which can be calculated in this particular context as

$$\text{Bias} = \sum_{j=1}^{l} \mathbf{y}_j - \mathbf{x}_j. \tag{4.2}$$

The low bias evident in Fig. 4.2 indicates that, on average, the maximum and minimum measured values are situated at an equal distance from the mean value derived from six measurements taken at each position across the entire field.
We conclude by examining the Pauli RGB images of the expansive maize field, which will be utilized in subsequent analyses. Fig. 4.3 depicts the images from flights 7 to 13, which provide the initial opportunity to classify the scatterers present. In flight 7, the field displays a greater degree of blue and purple hues, indicating a heightened presence of surface scatterers, which is consistent with the expectation for low vegetation. From flight 9 onwards, the field displays a greener hue, indicating an increase in volume scatterers. In flights 11 and 13, the field exhibits a distinctly reddish tone, suggestive of a rise in dihedral scatterers. The presence of green areas in these flights implies the continued presence of volume scatterers.

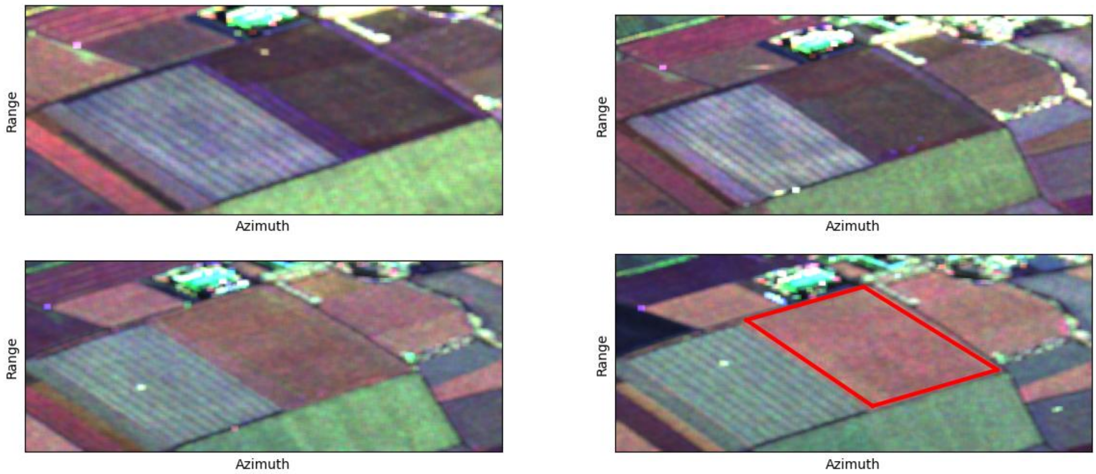

Figure 4.3: Pauli RGB images at L-Band of flight 7 (top left), flight 9 (top right), flight 11 (bottom left) and flight 13 (bottom right) of the big maize field marked in red from Fig. 4.1.

The following chapter presents the methodologies for the separation of the ground and volume layers from the data set, as well as potential approaches for the determination of soil moisture.

4.2 Two-step decomposition

The following section examines the two-step decomposition. The initial step is to formulate the problem of ground and vegetation separation as an SKP problem. The model is introduced, and the constraints are defined in a manner that allows a separation of ground and vegetation. Subsequently, the vertical profiles of the results are examined to ascertain whether they are ambiguous. Subsequently, the reconstruction error is examined to ascertain the degree of approximation achieved. Next, the ground-to-volume ratio of the results is examined, along with the implications of not setting the ground to zero height but allowing it to vary. Finally, the question of whether the resulting polarimetry matrix for the ground is truly a surface or dihedral scatterer is addressed.
In the second step, we investigate the potential for determining soil moisture values using H/α space derived from the physical models. To this end, we examine the H/α space of the X-Bragg and dihedral models with a view to identifying soil moisture from the resulting $\mathbf{T}_{ground}$ from the first step.

4.2.1 Ground and volume-layer separation

This section examines the initial step, which is the separation of the ground and volume layers. In this step, the multibaseline data feature is employed extensively, enabling the signal to be divided into two parts on the basis of the vertical information. The objective is to identify a separation of the signal that yields the desired layers, ensuring that the following equation is valid:

$$\mathbf{MPMB} \approx \mathbf{R}_{ground} \otimes \mathbf{T}_{ground} + \mathbf{R}_{volume} \otimes \mathbf{T}_{volume}, \tag{4.3}$$

with R_{ground} and R_{volume} as the structure matrices and T_{ground} and T_{volume} as polarimetry matrices for the corresponding layer.
In order to achieve this, we are required to make the same three assumptions as outlined in Section 3.1.
The next step is to calculate the decomposition. This can be achieved by converting the problem into an optimisation problem. One straightforward approach is to define the cost function as the difference between the data matrix and the decomposition

$$\min_{\mathbf{R}_i, \mathbf{T}_i} ||\mathbf{MPMB} - (\mathbf{R}_{ground} \otimes \mathbf{T}_{ground} + \mathbf{R}_{volume} \otimes \mathbf{T}_{volume})||. \tag{4.4}$$

The selected metric for measuring the discrepancy between the data and decomposition can be selected freely. However, going forward, the metric of choice is the classic matrix norm, the Frobenius norm, which is also employed by the original SKP method for optimal decomposition.
The aforementioned process can be optimised through the implementation of the algorithm delineated in Section 3.2. The optimisation method based on backpropagation optimises the same cost function as the original SKP decomposition. However, the results of this method fall within the solution space of the SKP decomposition, but there is a negative aspect associated with gradient-based iterative methods. Namely, the solution of backpropagation may be inferior (i.e. does not converge or remains at a local minimum) to that of SKP, depending on the initial parameters (e.g. the step size or the number of iterations).
As previously stated, the key benefit of the optimisation approach with backpropagation is its adaptability, including the integration of physical models, which is the subject of the following section.

Model

Constraints In order to separate the ground and volume components from the signal, it is necessary to make a few assumptions regarding the structure and polarimetry matrices. One such assumption is that the ground layer is at zero height, assuming that the data has been properly calibrated. This can be achieved, for example, by setting the structure matrix to height zero using a Dirac signal. The Dirac signal at height z can be generated by utilising the steering vector $\mathbf{h}(z) = (1, e^{-j\kappa_{z_2}z}, e^{-j\kappa_{z_3}z}, ..., e^{-j\kappa_{z_n}z})^T \in \mathbb{C}^n$ and forming the outer product with itself

$$\mathbf{R}_{ground} = \mathbf{h}(0)\mathbf{h}(0)^H = \begin{pmatrix} 1 & \dots & 1 \\ \vdots & \ddots & \vdots \\ 1 & \dots & 1 \end{pmatrix}. \tag{4.5}$$

The subsequent constraint pertains to the volume component, wherein the polarimetry matrix may be defined in accordance with the specifications outlined in section 2.1.2, encompassing the random, vertical, and horizontal oriented dipole scatterers.

Accordingly, the number of potential solutions has been reduced to those that exclusively seek the polarimetry matrix for the ground and the structure matrix for the selected volume polarimetry.

The next constraint ensures that the structure ($\mathbf{R}_{volume}$) and polarimetry ($\mathbf{T}_{ground}$, $\mathbf{T}_{volume}$) matrices are positive semi-definite (PSD). To do this we use the property of the product of a matrix with the conjugate transpose of itself - we know that for complex matrices the result is a hermitian matrix with real positive eigenvalues and is therefore PSD [16]. So we define

$$\mathbf{R}_{volume} = \mathbf{X}_{volume}\mathbf{X}_{volume}^H, \tag{4.6}$$

with $\mathbf{X}_{volume} \in \mathbb{C}^{n\times n}$ as the variable with which we construct the structure matrix for the volume, and we do the same with the polarimetry matrices ($\mathbf{T}_{ground}$, $\mathbf{T}_{volume}$).

The tomograms can now be evaluated to ascertain the extent of the resulting separation.

Resulting structure matrices The tomograms resulting from the decomposition process, obtained with different volume polarimetry matrices from Section 2.1.2, are now be examined on the example of the maize field shown in Fig.4.4 top-left corner, with particular attention to the area along the blue line. It should be noted that subsequent sections of this chapter are referring to this line.

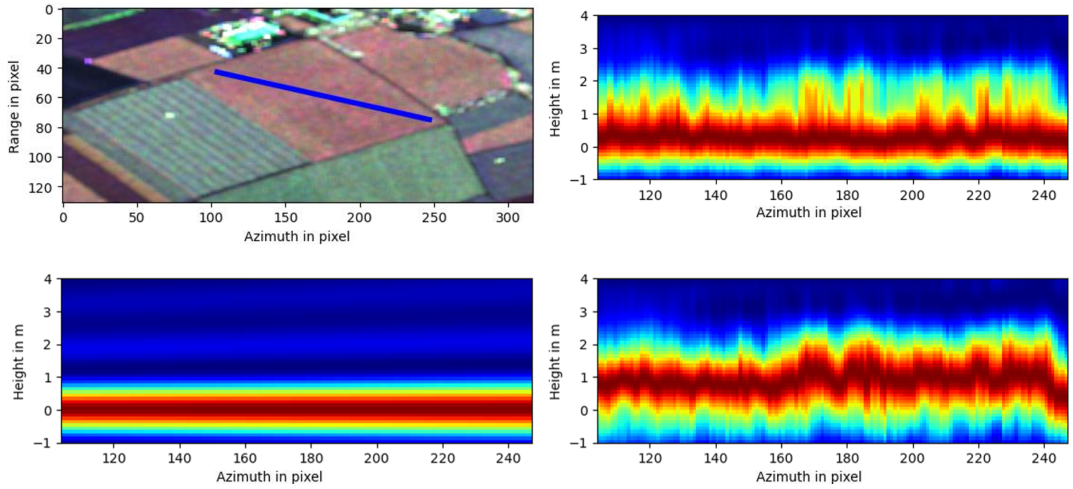

Figure 4.4: Pauli RGB image in L-Band of the examined maize field on flight 13 (top left). The corresponding blue line of the left-up image is presented in the form of a SAR tomogram (top right). SAR Tomogram of the resulting ground structure matrices (bottom left). SAR Tomogram of the resulting volume structure matrices with $\mathbf{T}_v^{(\mathrm{ran})}$ (Bottom right).

From the image, it can be observed that the red colour is the most prominent, which suggests that the dominant scattering mechanism is the Dihedral scattering. This is also evident in the top right-hand corner, where a tomogram can be observed in the $|S_{HH} + S_{VV}|$ Pauli basis, where there is minimal volume scattering. The results of the separation can be observed in the final two images, where the structure matrix of the ground is depicted in the lower left corner, fixed at a height of 0 as previously defined, and the structure matrix of the volume layer with a random volume polarimetry matrix is shown in the lower right corner. In this latter case, the ground is not visible in the signal, but only above height zero.
Given the expectation of disparate decomposition solutions for varying volume polarimetry matrices, it is prudent to direct our attention to these. Upon examination of the resulting tomograms Fig.4.5 of the volume structure matrices with oriented dipoles, no significant differences are evident. The random and vertical oriented dipoles for volume polarimetry matrices yield the most similar results of the three to each other. It can be concluded that, irrespective of the selected volume polarimetry matrix, the associated structure matrices remain consistent and thus provide an equally description of the vegetation.
It is important to consider whether the results are truly independent of the initial parameters, given that, as previously discussed, it is not always possible to ascertain

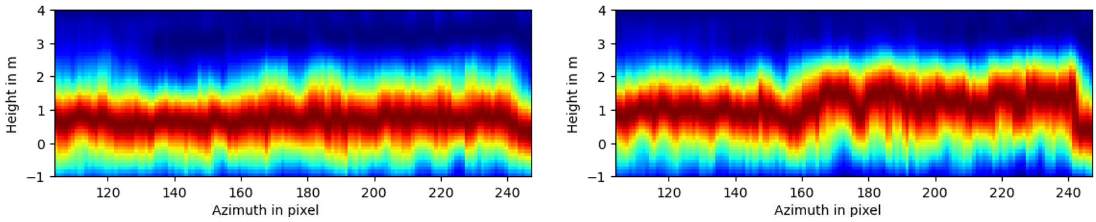

Figure 4.5: SAR Tomograms of the resulting volume structure matrices with horizontal (left) or vertical (right) oriented dipole scattering polarimetry.

whether the optimal outcome is achieved when solving non-linear problems. This is addressed and discussed next.

Ambiguity In this context, an ambiguous solution is defined as a result obtained when different solutions are produced for different initial parameters. This may occur due to insufficient iteration steps or the convergence towards a local minimum. Conversely, a unique solution is defined as the result that remains consistent regardless of the initial parameters. It can be observed that in the majority of analysed resolution cells, the solutions yielded unique results. In these cases, the anisotropy of the resulting $\mathbf{T}_{ground}$ matrices were always equal 1, which would indicate that the $\mathbf{T}_{ground}$ has rank 2. However, in the event that anisotropy was not equal to 1 and thus $\mathbf{T}_{ground}$ rank 3, the solution was ambiguous and anisotropy < 0.5 was applicable. This would suggest the presence of a significant third scattering mechanism. It is also noteworthy that the ambiguous parts were not identical for all volume polarimetry matrices and therefore dependent on the chosen $\mathbf{T}_{volume}$.
Next, we assess the degree of approximation between the decomposed data and the original data set.

Reconstruction error In order to assess the quality of the decomposition, we employ a metric based on the difference between the data and the decomposition obtained using the Frobenius norm, which also employs the defined cost function. However, in order to more accurately estimate the error and ensure its independence from the size of the data matrices, we employ the relative error

$$\text{Error} = \frac{||\mathbf{MPMB} - (\mathbf{R}_{ground} \otimes \mathbf{T}_{ground} + \mathbf{R}_{volume} \otimes \mathbf{T}_{volume})||_2}{||\mathbf{MPMB}||_2}. \tag{4.7}$$

A comparison of the relative error of the decomposition with different volume polarimetry matrices reveals that the SKP error is the lowest, with the predefined

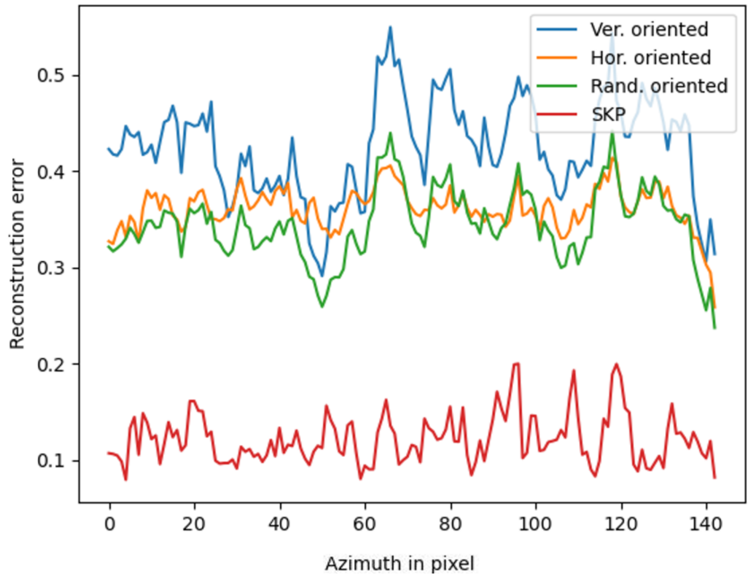

Figure 4.6: The reconstruction error for flight 13 with different volume polarimetry matrices is compared to the original SKP decomposition.

constraints resulting in a significantly larger discrepancy, as illustrated in Fig. 4.6. It is evident that the decomposition with a randomly oriented volume polarimetry matrix yields the most optimal results on constrained solutions, with results similar to those obtained with a horizontally oriented matrix. However, the vertically oriented volume matrices exhibit the greatest error.
An examination of the results of previous flights (Fig. 4.7) reveals a reduction in the SKP reconstruction error, which may be attributed to a decrease in the number or power of other scatterers. It is notable that the solutions employing ver/hor polarimetry matrices continue to exhibit a considerable degree of error. However, a noteworthy observation is that in previous flights, the error associated with the random oriented polarimetry matrix exhibited a decline, similar behaviour that is also observed with the SKP.
It is evident that the constraints exert a considerable influence on the error, which serves to illustrate that the standard SKP solution space differs greatly. The error can now be described in different ways. On the one hand, it indicates how well the data is approximated. On the other hand, the constrained decomposition can be regarded as a filter that removes any elements that cannot be described by the constraints (other SM not covered by the models). Therefore, while a large reconstruction error is not necessarily problematic, it is important to consider that

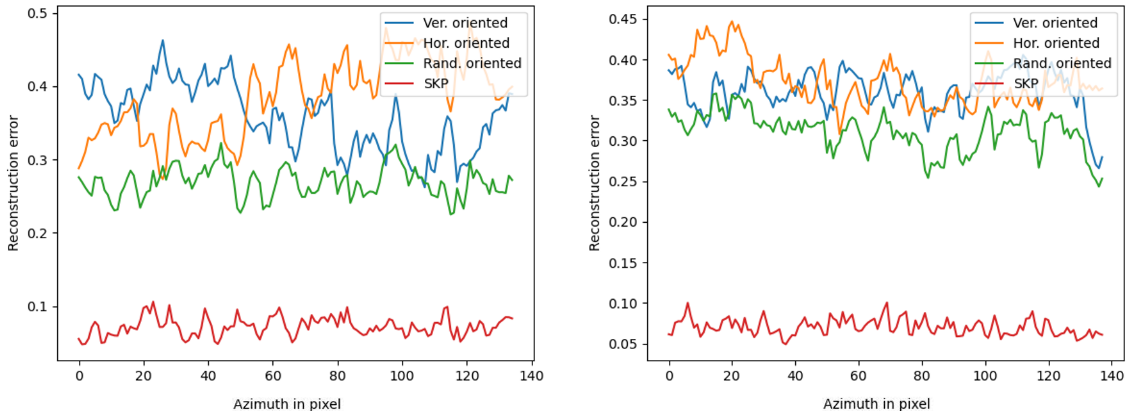

Figure 4.7: The reconstruction error for flight 9 (left) and flight 11 (right) with different volume polarimetry matrices is compared to the SKP decomposition.

the larger it is, the more influence it has on the parameters that are desired. It is crucial to recognise that the objective is to influence the model parameters in a manner that minimises the reconstruction error. This approach may result in the models attempting to describe undefined SM to the greatest extent possible, which could introduce errors. Consequently, the actual parameters may be influenced by this, which is why we have defined a component for the volume part and included it in the model, rather than omitting it.
An additional noteworthy parameter to examine is the ground-to-volume ratio of the resultant signals subsequent to decomposition.

Ground to volume ratio The ground-to-volume ratio $\frac{f_{ground}}{f_{volume}}$ provides insight into the strength ratio of the resulting ground and volume layers of the decomposition. To calculate this, it is first necessary to determine the strengths of the signals. This is achieved by employing the traces of the polarimetry and structure matrices

$$f_{ground} = \mathrm{trace}(\mathbf{R}_{ground}) \cdot \mathrm{trace}(\mathbf{T}_{ground}) \tag{4.8}$$

$$f_{volume} = \mathrm{trace}(\mathbf{R}_{volume}) \cdot \mathrm{trace}(\mathbf{T}_{volume}). \tag{4.9}$$

A review of the ratio in Fig. 4.8 reveals unexpected results for flight 9. The ground proportion is observed to be considerably lower than that of the volume, contrary to the expected outcome. The volume proportion is seen to be relatively high in most of the solutions, although the height of the vegetation at flight 9 is one metre, which is significantly lower than at flight 13 (3 m). One potential explanation for this discrepancy is that the low vertical resolution results in the phase centres of

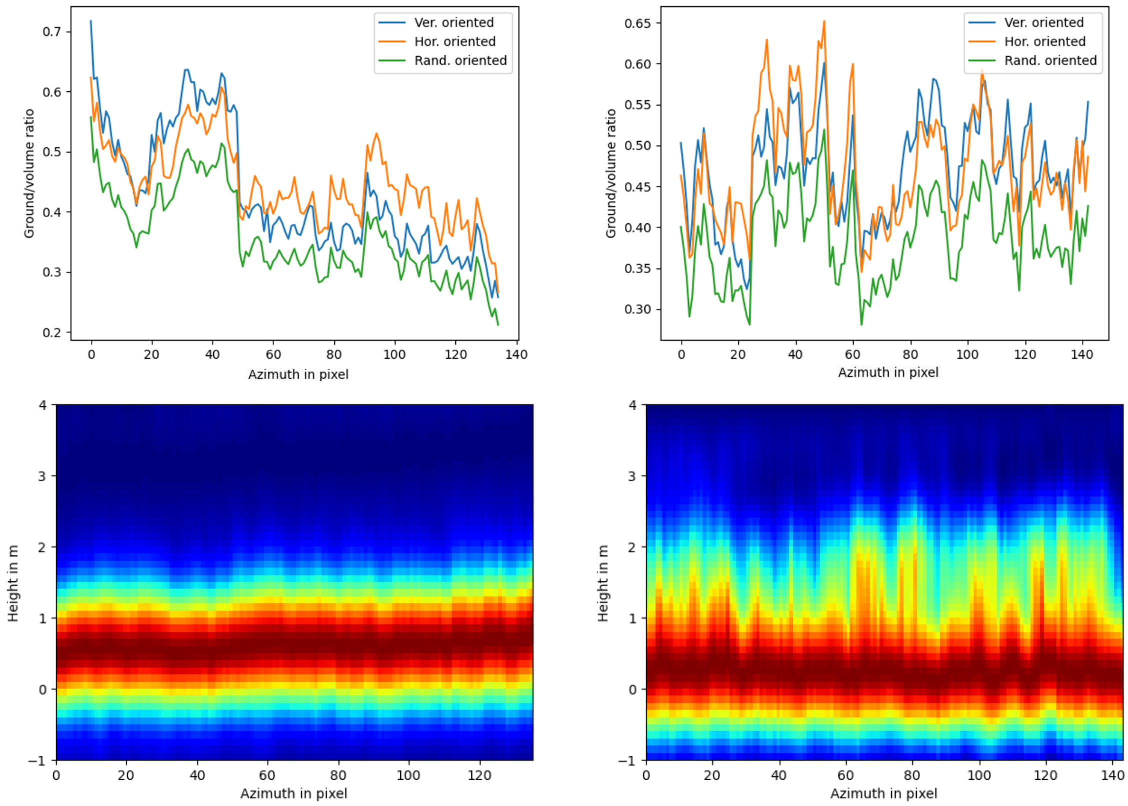

Figure 4.8: The ground/volume ratio of the resulting ground and volume layer for flight 9 (top left) and flight 13 (top right) and the corresponding tomograms under first entry of the Pauli basis.

the ground and volume being at the same height (as observed in the corresponding tomogram). Consequently, the phase centre of the ground is shifted upwards, resulting in an almost absence of signal at zero height. The selection of the volume polarimetry matrices also has an impact on the ratio. It can be observed that the proportion of the ground is lower with randomly oriented volume than for vertically/horizontally oriented ones. This could also indicate that the randomly oriented polarimetry matrix is able to better approximate the volume or, at the very least, has a higher proportion in the signal than vertically/horizontally oriented scatterers.

However, an examination of flight 13 reveals that the soil fraction remains low, which is to be expected given the higher vegetation. Furthermore, the ground fraction is observed to be lower when a random oriented polarimetry matrix is employed than when a vertical/horizontal oriented matrix is used. Nevertheless,

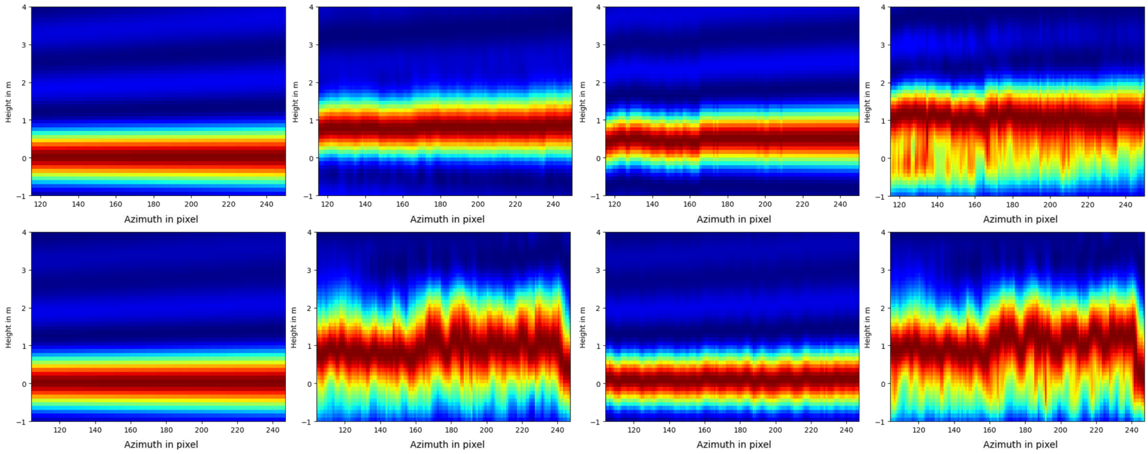

Figure 4.9: The resulting tomograms of the structure matrices for ground and volume for flight 9 (first row) and 13 (second row) with fixed ground (the initial two columns) and variable ground height (the final two columns) are presented herewith.

the results are also quite similar for vertical/horizontal oriented volumes, indicating that there is not a significant difference in the use of either for the ground to volume ratio.

Finally, we shall examine the constraint in which the structure is fixed to the ground and investigate the consequences of continuing to use a Dirac signal, but with a variable height.

Variable Dirac height for ground The constraint for $\mathbf{R}_{ground}$ is now relaxed for this investigation by allowing not only a signal at zero height. This is achieved by defining the ground structure matrix in a manner similar to that previously described, with the assistance of the steering vector $\mathbf{h}(z)$, but with variable height

$$\mathbf{R}_{ground}(z) = \mathbf{h}(z)\mathbf{h}(z)^H. \tag{4.10}$$

This examination is of particular interest as the data used are not fully calibrated, which may result in a shift in the vertical profile and the assumption of ground at height zero being invalid. Furthermore, it could be of interest to note that the phase centres could potentially overlap with ground and vegetation due to the relatively small vertical resolution (i.g. 1 m for flight 13).

Upon examination of the resulting tomograms in Fig. 4.9, it becomes evident that there are no significant discrepancies between the fixed and variable ground conditions in flight 13. It can be observed that the height of the Dirac signal undergoes

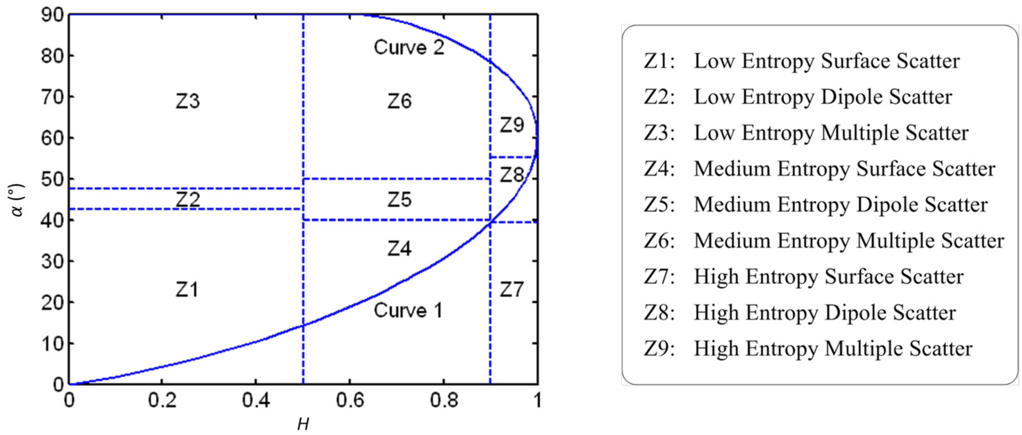

Figure 4.10: H/α plane with corresponding SM [17].

slight alterations when the ground is variable. This leads to the conclusion that the cost function is at its minimal value when the height is zero. However, this is not the case in flight 9, where the tomograms for the ground and volume are markedly disparate. In particular, at variable height, the phase centre is observed to exceed zero for the minimum cost function. This naturally gives rise to the question of the extent to which the ground and volume layers can be separated vertically in flight 9.

The vertical structure has now been examined with the aid of tomograms in order to investigate the decomposition result. An alternative approach would be to examine the resulting $\mathbf{T}_{ground}$ component with the help of EVD from Section 2.1.1, with a view to determining which scatterer it represents.

H/α space of $\mathbf{T}_{ground}$

In the following section, we undertake a more detailed examination of $\mathbf{T}_{ground}$, with the objective of identifying the scatterer in question. This can be achieved through the utilisation of entropy and α angle.

Figure 4.10 illustrates the ranges for entropy and alpha values and the corresponding SM. These can be used to ascertain which SM is involved in $\mathbf{T}_{ground}$.

A review of the H/α from $\mathbf{T}_{ground}$, as illustrated in the preceding examples for flight 13 (Fig. 4.11), reveals that the majority of them fall within the range of dihedral scatterers. However, it is noteworthy that they are situated in close proximity to the threshold of volume scatterers. Furthermore, the solutions of the selected volume polarimetry matrices exhibit a minimal distinction in alpha angle ranges, with the

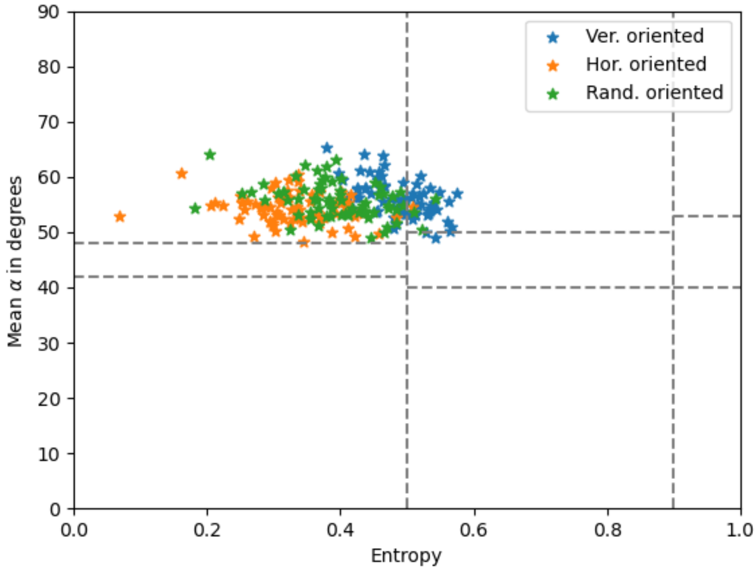

Figure 4.11: H/α of the resulting T_{ground} for flight 13 with different volume polarimetry matrices.

entropy demonstrating a more pronounced variation.

An examination of the earlier flights in Fig.4.12 reveals that in flight 11, the values exhibit a greater shift towards the volume range, although they remain predominantly within the dihedral. However, in flight 9, a notable transition is observed, with a significant portion of the data now falling within the volume range and exhibiting characteristics of surface scatterers. This is an anticipated outcome, given the reduced vegetation coverage. The variation of the solutions for alpha depending on the chosen volume polarimetry matrices remains within a similar range. Of note is the reduction in range for entropy at flight 9, indicating minimal difference between the chosen volume polarimetry matrices. (This aligns with the hypothesis that vegetation density is inversely proportional to the number of volume scatterers.)

In the case of variable height, it can be observed that the entropy and alpha angle properties exhibit similarities and do not display significant discrepancies. However, it is notable that the entropy value may exhibit fluctuations in instances where small vegetation is present.

Having completed an examination of the initial phase of the decomposition of the ground and volume layers, and having ascertained that the resulting data is of an acceptable standard for $\mathbf{T}_{ground}$, we now proceed to the next stage of the process,

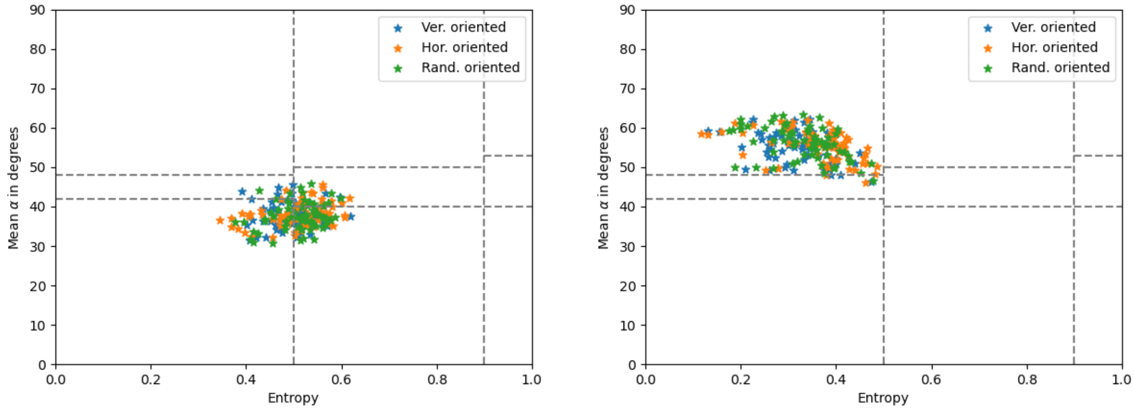

Figure 4.12: H/α of the resulting $\mathbf{T}_{ground}$ for flight 9 (left) and flight 11 (right) with different volume polarimetry matrices.

which involves the utilisation of physical models in order to extract pertinent physical information from $\mathbf{T}_{ground}$.

4.2.2 Fitting of polarimetric models for ground scatterer

In the second step, the objective is to ascertain the geophysical parameters from the resulting $\mathbf{T}_{ground}$ by employing physical models from section 2.1.2. Given that the physical models are constituted by non-linear equations, it is only feasible to solve them directly in exceptional cases, as there exists likely no closed form of the solution. One potential approach to solving the equations is to employ optimization techniques.
Alternatively, one could leverage the H/α space previously utilized to identify the scatterer in question. This would facilitate the establishment of a link between the geophysical parameters and H/α space through the calculation of all potential constellations of the physical models and their corresponding H/α. This can then be employed with the assistance of lookup tables.

X-Bragg scattering model

We shall commence with an examination of the X-Bragg model from section 2.1.2, together with the H/α associated with it. First, we define the ranges of the variables with regard to physical properties:

- Dielectric constant of soil: $\varepsilon_s \in [3, 25]$

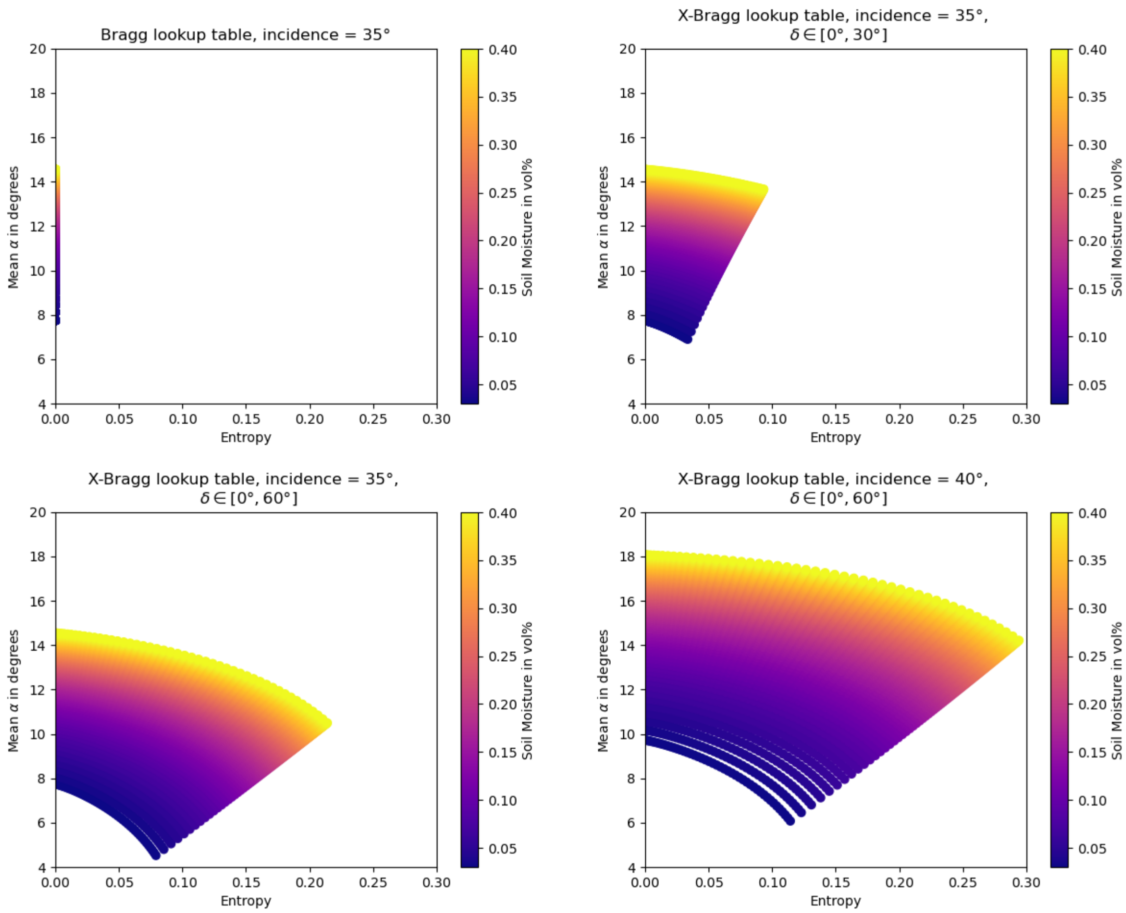

Figure 4.13: Bragg and X-Bragg lookup tables with varying parameters.

- Depolarization Parameter: $\delta \in [0°, 60°]$
- Incidence angle: $\theta = 35°$

The dielectric constant ε_s was chosen so that it reflects the range for soil moisture between 3 vol% and 40 vol% [18]. The incidence angle depends on the SAR data recordings and the parameter for depolarisation is allowed to be in the range $[0°, 90°]$, but 60° is chosen as the maximum angle to exclude strong depolarisation. To begin, we examine the specific case of $\delta = 0°$, which transforms the X-Bragg model into the Bragg model. As illustrated in Fig. 4.13, the potential H/α region is relatively limited in extent, comprising a single line. This can be attributed to the fact that the polarimetry matrix of the Bragg model possesses only a rank of 1, resulting in an entropy value of 0 for all combinations of parameters. This demonstrates that the Bragg model is insufficient for accurately describing more complex scatterers on its own.

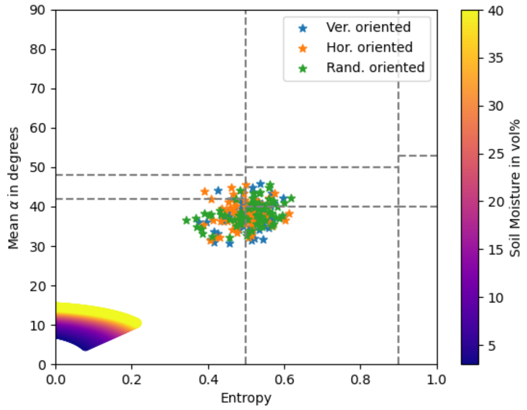

Figure 4.14: Soil moisture estimation with help of X-Bragg lookup table for flight 9 (left) and 13 (right).

Therefore, if we now consider the X-Bragg model with $\delta \geq 0°$ then the lookup table looks like Fig. 4.13. It can be observed that the valid range increases in proportion to the range of δ, which allows for a more comprehensive description. Furthermore, an increase in incidence angle results in an expansion of the valid range, albeit with a concomitant shift in the distribution of valid points, leading to a reduction in the number of valid points for very small H/α.

However, there are inherent limitations to this approach, particularly when considering Fig. 4.10, which illustrates that low entropy surface scatterers can only be described within this framework. A determination of the last resulting $\mathbf{T}_{ground}$ with the assistance of the aforementioned lookup table is not feasible, as the requisite geophysical parameters are not within the permissible range (Fig. 4.14). However, this behaviour is also anticipated on the basis of the assumption that dihedral scattering occurs on the ground layer over vegetated areas.

The next stage of the analysis entails an examination of the lookup table utilising the dihedral model.

X-Bragg plus dihedral scattering models

As demonstrated in the preceding section, the X-Bragg model is incapable of adequately describing the resulting $\mathbf{T}_{ground}$ in H/α space. This is due to the fact that there is evidence to suggest the presence of dihedral scatterers, which were also observed in the Pauli image. It is important to note, however, that if we consider the dihedral model in a standalone manner, we encounter the same issue as with

the Bragg model in alpha space. This is because the dihedral model can only describe entropy equal to zero, given that it also has rank equal to one. Consequently, the following section examines the X-Bragg and dihedral models in conjunction to address the issue of the resulting polarimetry matrix for the surface having a rank exceeding 1, thereby enabling a more expansive valid range in H/α space.
In order to proceed, it is first necessary to define the ranges of the model variables.

- Dielectric constant of soil: $\varepsilon_s \in [3, 25]$
- Dielectric constant of stem: $\varepsilon_t \in [20, 40]$
- Depolarization Parameter: $\delta \in [0°, 60°]$
- Incidence angle: $\theta = 35°$
- Parameter for a differential propagation phase: $\varphi \in [-60°, 60°]$
- Power proportion: $f_p \in [0, 1]$

The specific parameters of the dihedral model must now be added. These include the dielectric constant of the maize stem ε_t, which should be approximately in this range for maize with a high water content according to [19]. The parameter φ represents the differential propagation phase, which is caused by the vegetation. Given that we are now examining the sum of two components, the signal power of the model is no longer inconsequential, as it was previously. This is because the proportion of the signal allocated to each model is now a significant factor. This can be described by the following relationship:

$$\mathbf{T}_{\text{X-Bragg + Dihedral}} = f_p \mathbf{T}_{X-Bragg} + (1 - f_p)\mathbf{T}_{Dihedral}. \tag{4.11}$$

This $\mathbf{T}_{\text{X-Bragg + Dihedral}}$ is now employed in order to calculate the H/α for the new lookup table, as shown in Fig. 4.15.

X-Bragg plus dihedral It is evident that the models, when considered collectively, are capable of encompassing a considerably larger region within the H/α space domain. This arc is generated by different power factors f_p. In the lower left quadrant, the sequence begins with X-Bragg ($f_p = 1$), then goes up with decreasing f_p, and ultimately end with the pure dihedral model ($f_p = 0$). Furthermore, the separation observed at the point where the dihedral power is predominant is accompanied by an additional division of soil moisture regions. These arise due to

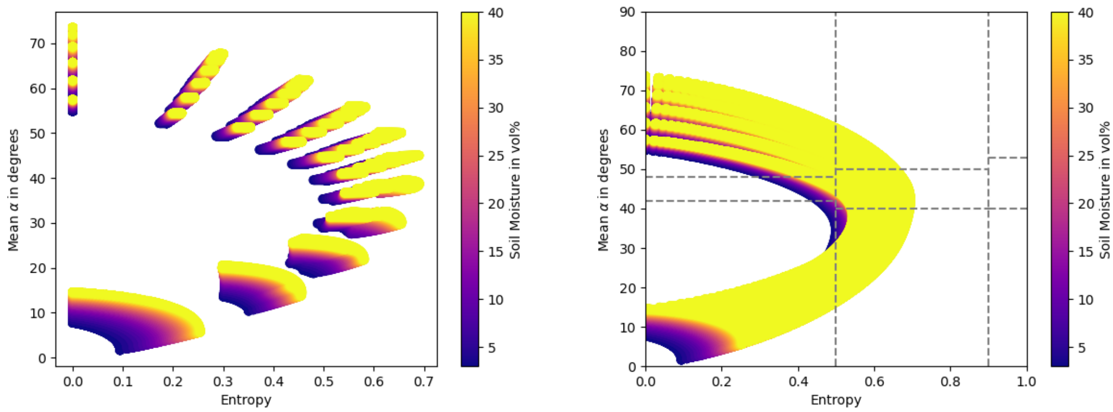

Figure 4.15: X-Bragg plus dihedral H/α space with 11 (left) and 150 (right) equidistant points of f_p.

the influence of different φ values. However, a new issue emerges: the H/α ranges of different parameters overlap, making it impossible to create a lookup table. This is because, as illustrated in the Fig. 4.15, a specific point in the H/α range yields numerous soil moisture values that fit.

It is noteworthy that polarimetry matrices can be generated using X-Bragg and dihedral (approximately for $f_p \in [0.3, 0.6]$), which together resemble a volume scatterer.

A method for reducing the extent of the overlapping regions is to utilise a simplified model for surface scattering , which is achieved by restricting the solutions to those with $\delta = 0°$.

Bragg plus dihedral By focusing on the case $\delta = 0°$, the X-Bragg model is reduced to the Bragg model. Upon examination of the H/α space depicted in Fig. 4.16, it becomes evident that the Bragg and dihedral models do not generate planes, but rather lines that are shifted for different values of f_p. It should be noted that the issue of overlapping due to φ is not resolved. However, if we fix φ, for example, to $\varphi = 0°$, we obtain a larger area that can be utilised for soil moisture estimation. Nevertheless, there is still an overlap in the range of values for approximately $f_p \in [0.5, 0.7]$. Furthermore, the restriction introduced reduces the valid range of the models in H/α space.

In the following section we investigate whether the latest iteration of the Ground model (X-Bragg + dihedral) offers any enhancements over only X-Bragg.

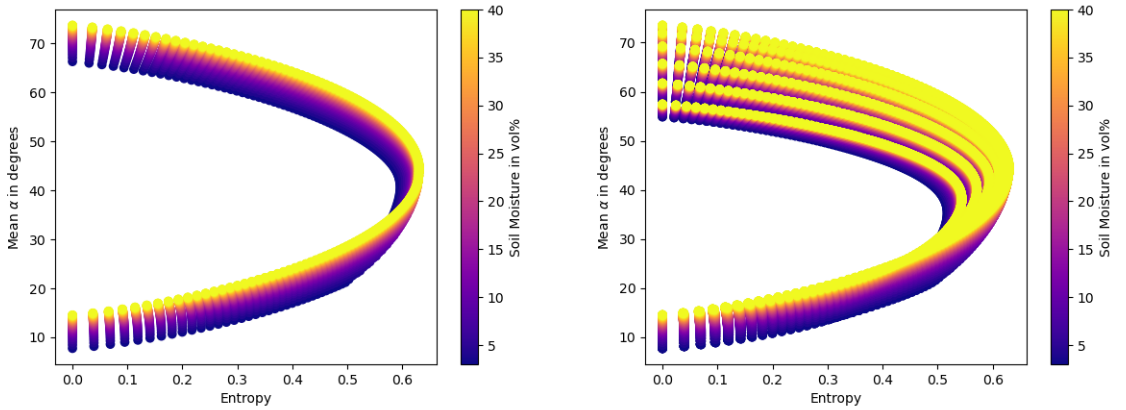

Figure 4.16: Bragg plus dihedral H/α space with $\varphi = 0^\circ$ (left) and 12 equidistant points in $\varphi \in [-60^\circ, 60^\circ]$ (right).

Experiments As illustrated in Fig. 4.17, the incorporation of the dihedral has significantly expanded the permissible range. This indicates that the majority of H/α derived from $\mathbf{T}_{ground}$ are now within the valid range of the model, irrespective of the selected volume polarimetry matrices. It should be noted that for flight 9, there is still a considerable amount of solutions that cannot be accounted for by the models. As previously observed with regard to the ground-to-volume ratio, the determined $\mathbf{T}_{ground}$ matrices are likely to be invalid due to insufficient vertical resolution. While it is theoretically possible to identify matching soil moisture values for flights 11 and 13, the ambiguity of the models precludes the identification of a single soil moisture value for each point. However, by focusing on specific solutions by introducing constraints, it becomes evident that the model is unable to describe a significant number of points.

As has been demonstrated, the ground and volume layer can be successfully separated using the introduced two-step decomposition. Furthermore, we demonstrated this with illustrative examples. However, the estimation of soil moisture proved to be unsuccessful. Two significant challenges emerge from this analysis. Firstly, the ambiguity of the solution is a consequence of the models themselves. Secondly, the range of applicability of the models is limited by the inclusion of points that fall outside the scope of their description. The initial issue was addressed through the imposition of constraints, which resulted in an expansion of the regions where the solution could be unambiguously determined. However, this approach necessitated a reduction in the permissible range. The subsequent methodology addresses these challenges by introducing supplementary constraints

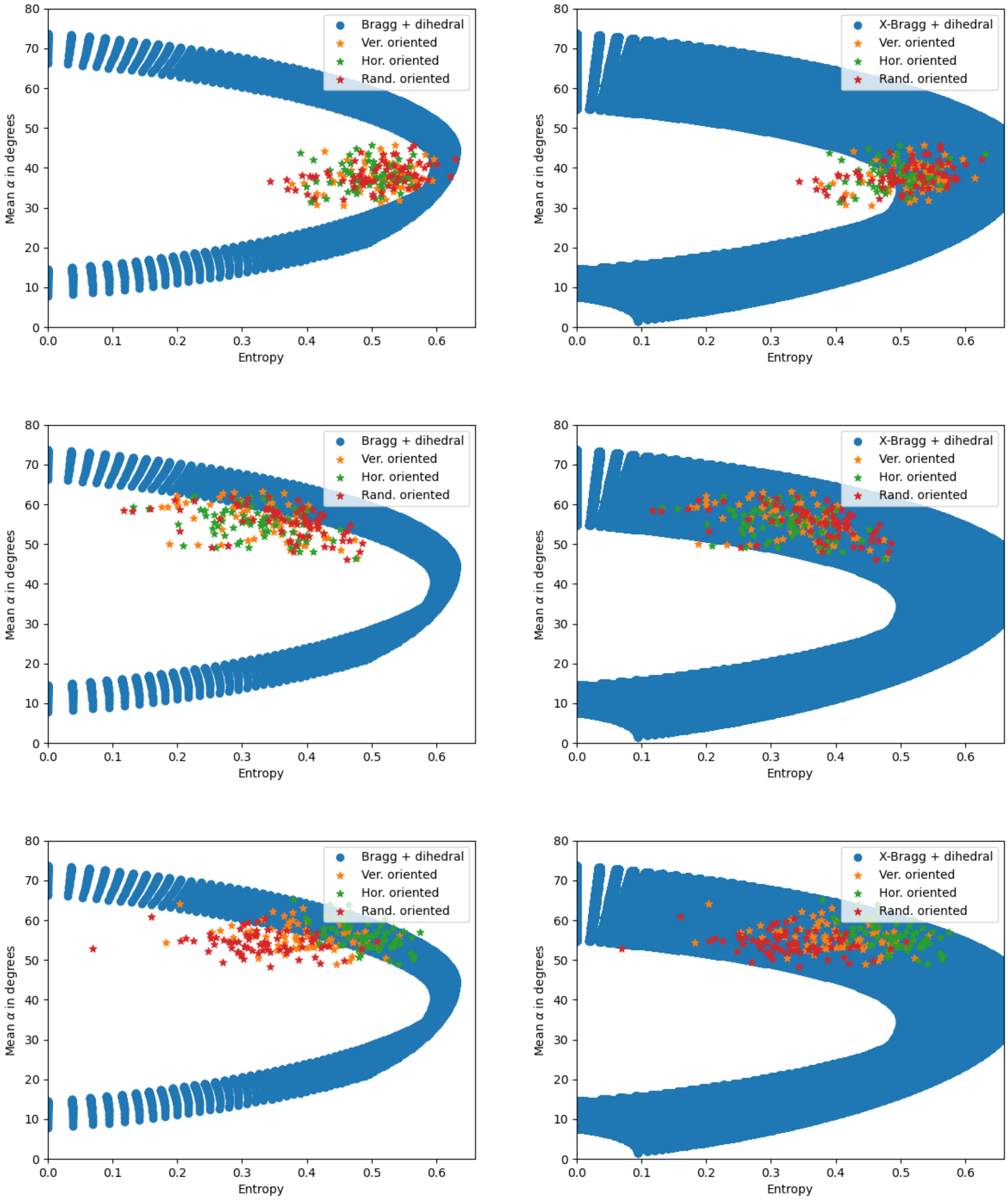

Figure 4.17: The resulting H/α of $\mathbf{T}_{ground}$with the valid ranges for constrained with $\varphi, \delta = 0^\circ$ (left) and unconstrained (right) X-Bragg and dihedral H/α space for flights 9 (first row) , 11 (second row) and 13 (third row).

and integrating physical models directly into the optimisation process, ensuring that only solutions that can be accurately described by the models are obtained.

4.3 One-step decomposition

We now turn our attention to the one-step decomposition. The X-Bragg and dihedral models are integrated into the SKP decomposition, and it is demonstrated that there are no unique solutions in the absence of additional constraints. Subsequently, we demonstrate that additional constraints can be employed to ascertain the soil moisture content, and present the resulting data and associated accuracy metrics. We then illustrate that the proposed approach indeed yields unique solutions. Additionally, we examine the magnitude of the reconstruction error and the ground-to-volume ratio of the results. Finally, we conduct a detailed analysis of the cost function and the influence of the physical model's parameters on the determination of the soil moisture.

4.3.1 Model

The data decomposition is now performed in a single step by incorporating the physical models into the optimisation process. The objective remains to identify a decomposition that satisfies the (4.3) equation. However, in this approach, $\mathbf{T}_{ground}$ is defined as the sum of the X-Bragg and Dihedral models ($\mathbf{T}_{ground} = \mathbf{T}_{X-Bragg} + \mathbf{T}_{Dihedral}$). Therefore, $\mathbf{T}_{ground}$ is no longer a free variable but is constrained by the structure of the physical models. For the purposes of clarity, we define $\mathbf{T}_{ground}$ as a function

$$\mathbf{T}_{ground} : \mathbb{R}^6 \rightarrow \mathbb{C}^{3\times3} : (\varepsilon_s, \varepsilon_t, m_s, \sigma, \delta, \varphi) \rightarrow \mathbf{T}_{X-Bragg}(\varepsilon_s, m_s, \delta) + \mathbf{T}_{Dihedral}(\varepsilon_s, \varepsilon_t, \sigma, \varphi). \tag{4.12}$$

The structure Matrix $\mathbf{R}_{ground}$ is still defined as an outer product of steering vectors on height zero (4.5) and $\mathbf{R}_{volume}$ as an outer product of a matrix with itself (4.6) . This allows us to define the new optimisation problem as:

$$\min_{\varepsilon_s, \varepsilon_t, m_s, \sigma, \delta, \varphi, \mathbf{R}_{volume}} ||\mathbf{MPMB} - (\mathbf{R}_{ground} \otimes \mathbf{T}_{ground}(\varepsilon_s, \varepsilon_t, m_s, \sigma, \delta, \varphi) + \mathbf{R}_{volume} \otimes \mathbf{T}_{volume})||. \tag{4.13}$$

Now, it is not the matrix $\mathbf{T}_{ground}$ itself that is calculated; rather, the physical parameters of the X-Bragg and dihedral models. As a result, the overall number of optimised variables is reduced from $9 + n^2$ to $6 + n^2$. In order to conduct a more detailed analysis, it is first necessary to define the ranges of the model variables that are physically meaningful, as was done previously:

- Dielectric constant of soil: $\varepsilon_s \in [3, 25]$
- Dielectric constant of stem: $\varepsilon_t \in [20, 40]$
- Depolarization Parameter: $\delta \in [0°, 60°]$
- Incidence angle: $\theta = 35°$
- Parameter for a differential propagation phase: $\varphi \in [-60°, 60°]$
- Parameter for powers: $m_s, \sigma \in \mathbb{R}^+$

Ambiguity

As evidenced by the two-step decomposition, the results are ambiguous. Moreover, the integration of the models did not yield the anticipated outcome, as an examination of the optimization parameters during optimization (Fig. 4.18) revealed that not all values converge to a single value. For instance, it can be observed that the strengths of X-Bragg and dihedral predominantly converge into a specified range. This could indicate that the cost function is essentially flat within this region, suggesting the presence of a low gradient. The behaviour of the power for the volume is distinct. It can be observed that the solution exhibits a tendency to oscillate between three local minima. This phenomenon can also be observed when examining the reconstruction error, which is the cost function, as there are also three minima. However, when analysing the parameters ε_s and δ, it becomes evident that the values only converge at the edges of the permissible solution. This indicates that it is not feasible to determine soil moisture values under these conditions.
It is also noteworthy that the resulting ground-to-volume ratio is approximately equivalent to that observed in the two-step decomposition previously illustrated.
As has been demonstrated, the incorporation of the physical models into the optimisation process facilitates the attainment of solutions that align with the physical models themselves. However, the issue of determining the soil moisture values remains unresolved. The subsequent challenge that emerged was the lack of sensitivity of the optimisation problem to the soil moisture. This can be addressed by introducing new constraints to the powers of the physical models for X-Bragg and dihedral, which is done subsequently.

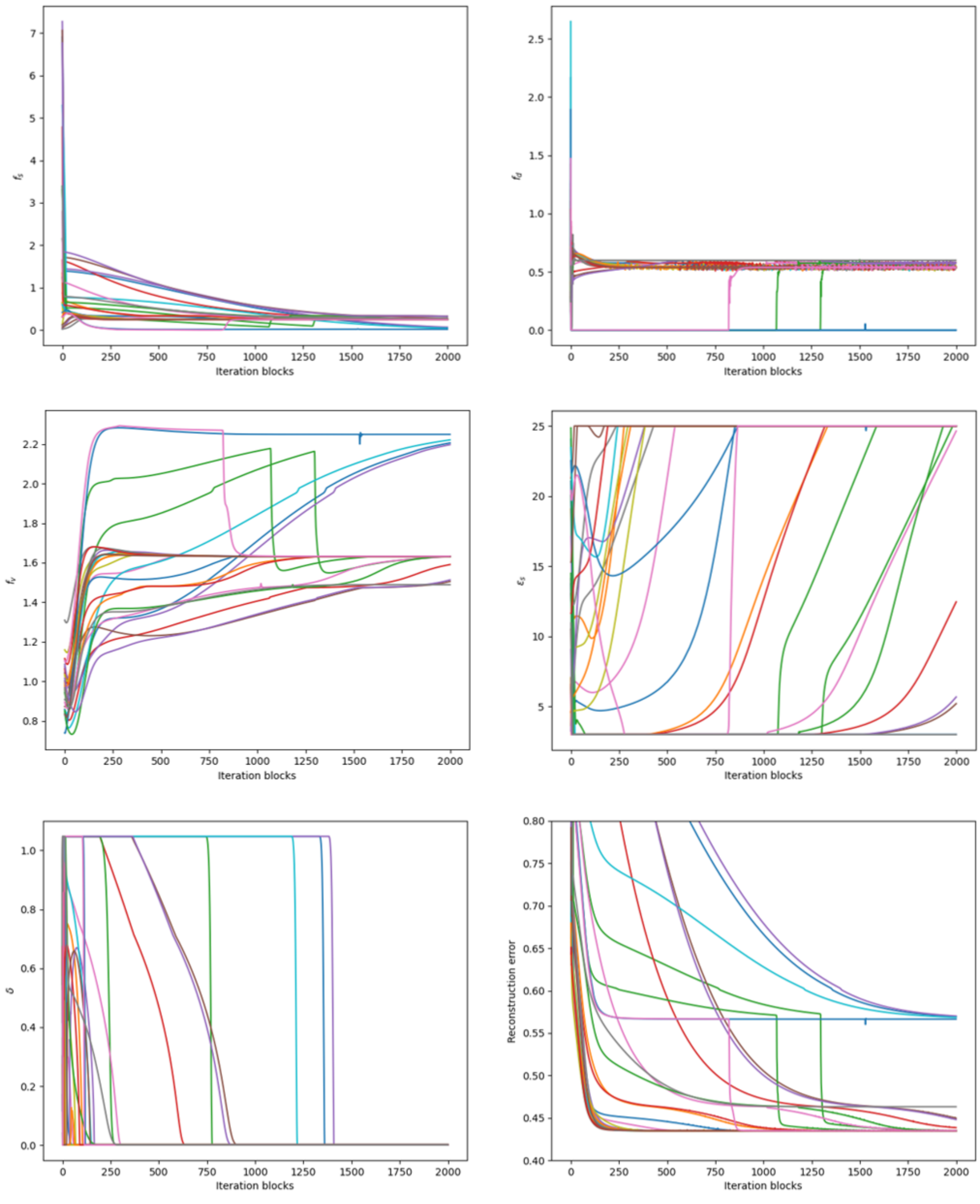

Figure 4.18: The convergence behaviour of the optimisation parameters at a concrete field point, based on the results of 28 different runs (different colour) with vertical oriented dipoles for the volume polarimetry matrix.

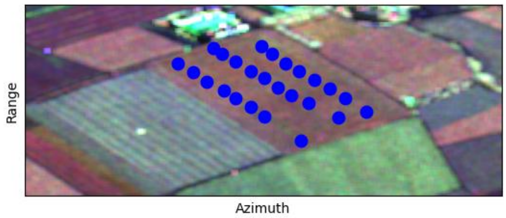

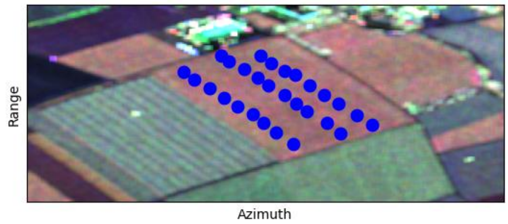

Figure 4.19: The locations of measured soil moisture values in blue for flight 11 and 13.

4.3.2 Soil moisture estimation

The following section addresses the issue of soil moisture estimation directly. In order to facilitate the evaluation of the estimated moisture values, the locations of the measured moisture are now presented in Fig. 4.19 for the sake of clarity for flight 11 and 13.
As previously stated, it is necessary to introduce supplementary constraints for the parameters m_s from X-Bragg and σ from dihedral model (for the power parameter) in order to achieve an unambiguous and acceptable determination of soil moisture values. These additional constraints are:

- Flight 13:
  - $m_s \in [0.187, 0.2]$
  - $\sigma \in [0.042, 0.052]$
- Flight 11:
  - $m_s \in [0.192, 0.2]$
  - $\sigma \in [0.042, 0.056]$
- Polarimetry matrix for volume: $T_v^{(\text{ver})}$

As can be observed, the currently accepted range for these parameters is relatively narrow, yet was selected to yield more accurate estimated soil moisture values. However, as the parameters are loosened, the results remain satisfactory for specific points, but the overall results deteriorate until the initial problem is encountered, whereby soil moisture is no longer a significant factor for the cost function. It is also noteworthy that the ranges were derived through a process of trial and error, rather than through the application of a direct algorithmic approach.

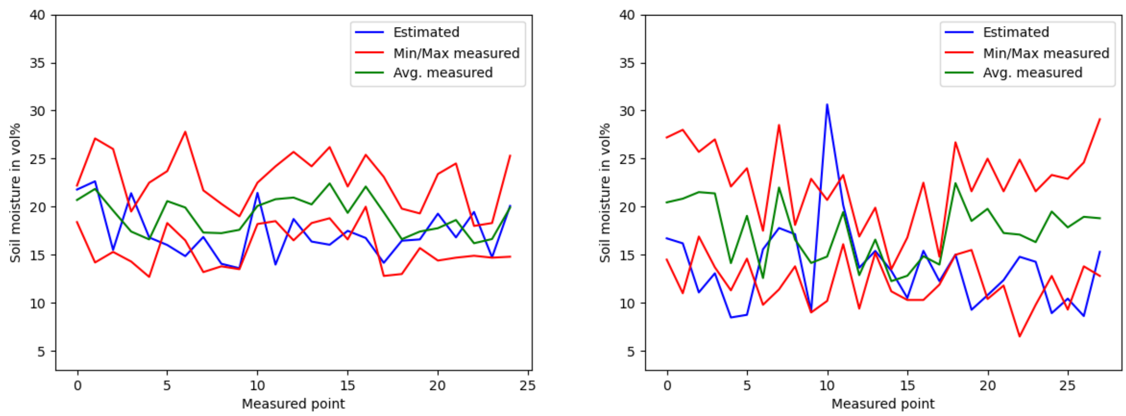

Figure 4.20: The comparison of estimated and measured soil moisture values for flight 11 (left) and 13 (right).

The application of additional restrictions yields estimated soil moisture values, as illustrated in Fig. 4.20. It is evident that the soil moisture can now be determined with minimal deviations. It should be noted that the solution may vary depending on the volume polarimetry matrix in question, and that the parameters may require adjustment in such cases. To objectively assess the performance of the estimation, statistical values are now examined.

Soil moisture estimation error

As illustrated in Fig. 4.21, the estimation exhibits a bias of −2.7 vol%, indicating that the calculated values are typically lower than the average measured values. Of note is the relatively low RMSD value, which is not significantly larger than by the measured values deviation. This suggests that the observed deviation is approximately consistent with the ground measurements.
It can be reasonably deduced that this is the closest approximation to the actual values that can be obtained statistically. This is due to the necessity of accounting for the deviation of ground measurements on the one hand and, on the other, the fact that the dataset covers a considerable area, which may already exert a significant influence on the estimation of a point due to the potential for considerable changes in soil moisture.
In light of the aforementioned constraints, it is now necessary to consider how the behaviour of convergence has been affected and whether the solution is now unique.

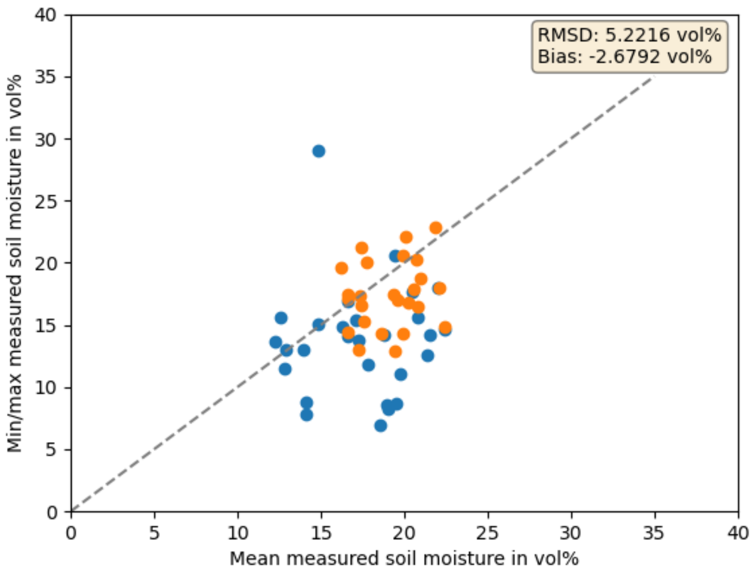

Figure 4.21: Deviation of the estimated to the measured soil moisture values for flight 11 (orange) and flight 13 (blue).

Convergence

The introduction of additional constraints ensures that the solution is unique and converges to a specific value. As illustrated in Fig. 4.22, which considers the same point as in Fig. 4.18, the δ and ε_s parameters now also converge within the valid range. The new powers also exhibit convergence within a similar range, irrespective of the constraints. Furthermore, the power for the volume now also demonstrates convergence to a comparable value. The positive outcome is that convergence is achieved in a shorter number of iterations than without constraints. However, as can be observed, the new solution is not a normal local minimum; rather, it is a new minimum created through the constraints. This has the consequence that certain parameters, such as in this case the powers of X-Bragg and dihedral, cannot increase or decrease arbitrarily. However, it is evident that the solution no longer represents the best fit to the data, as evidenced by the increased reconstruction error compared to the unconstrained solution.

Having established that the solutions are both convergent and unique for the specified points subject to the aforementioned constraints, we now turn our attention to the constraints imposed on the resulting powers. To this end, we utilise the ground-to-volume ratio as a means of quantifying the extent of these constraints.

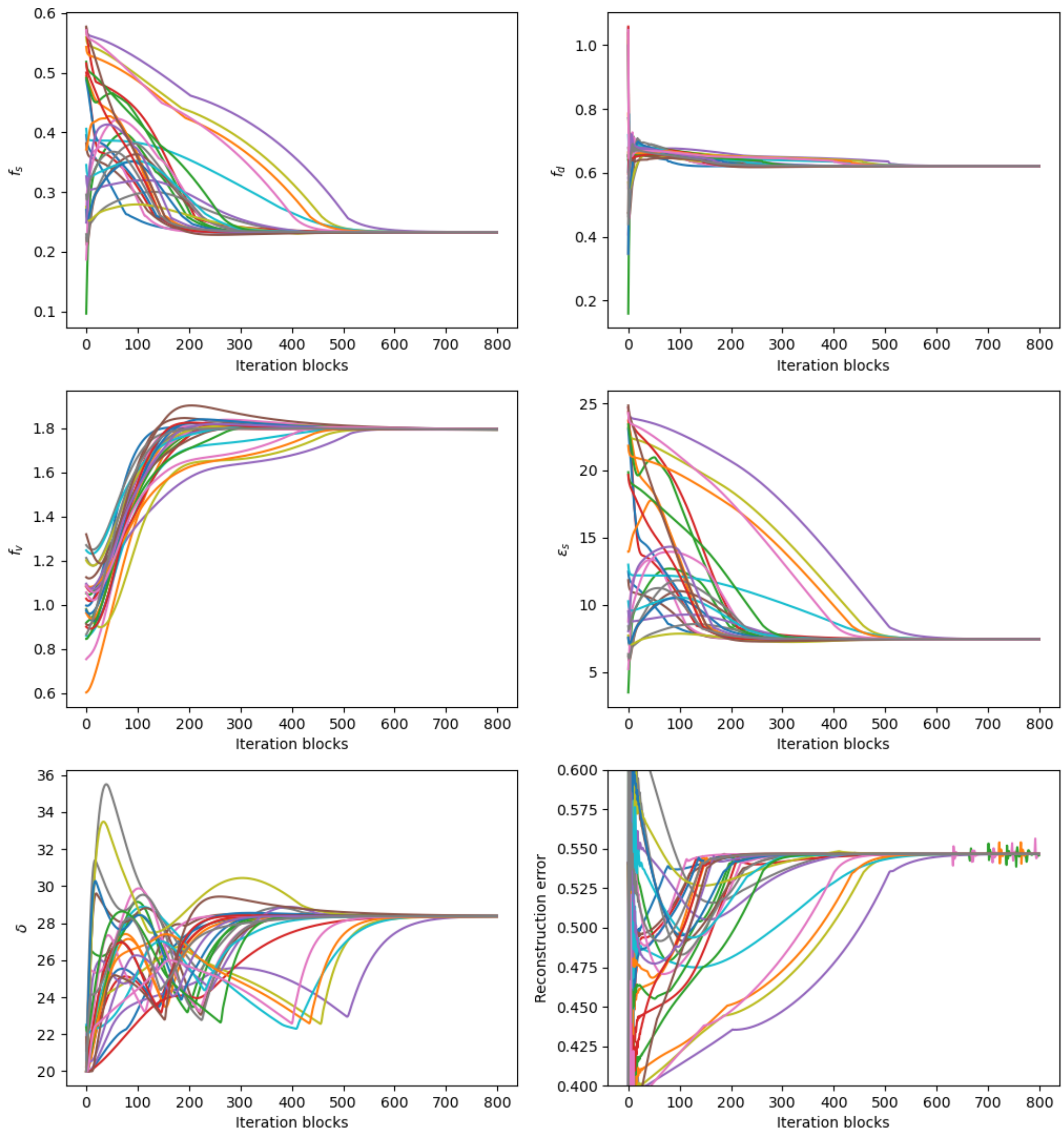

Figure 4.22: The convergence behaviour of the optimisation parameters at the same field point as in Fig. 4.18, based on the results of 28 different runs (different colours).

Ground-to-volume ratio

As illustrated in Fig. 4.23, the constraints do not exert a significant influence on the resulting powers, contrary to expectations based on the limited defined ranges. In the results for flight 13, there is minimal differentiation between the ranges of values. However, in flight 11, the picture is markedly different. The ground power, which is composed of X-Bragg and dihedral, typically exhibits considerably higher values for the unconstrained variant than the constrained. It can be surmised that

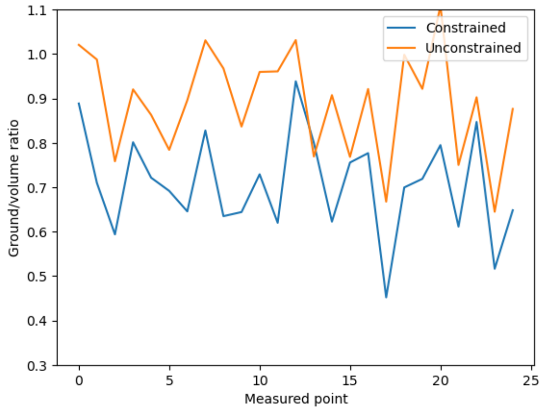

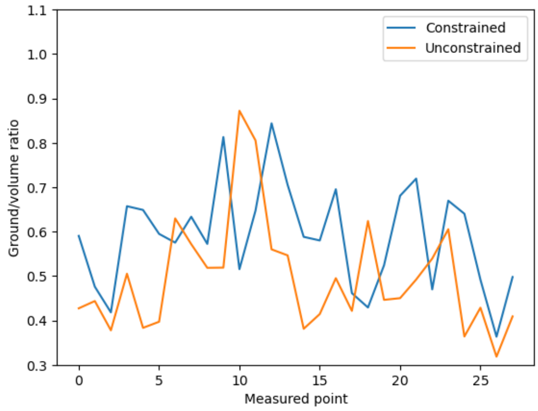

Figure 4.23: The ground-to-volume ratio of the decompositions with added constraints and without added constraints for flight 11 (left) and 13 (right).

the effective range of the ground power with constraints is being approximated shown here. It is clear that for the majority of points, the ground-to-volume ratio is between 0.5 and 0.7 for both flights. However, this pattern is not evident in the unconstrained approach.

Finally, we examine the manner in which the reconstruction error alters in conjunction with the constrained variable, with the objective of determining the extent to which the novel solutions diverge from the unconstrained in terms of the cost function.

Reconstruction error

As illustrated in Fig. 4.24, the unconstrained solution does not invariably exhibit the lowest error. It is evident that the solutions obtained from the unconstrained approach are inherently ambiguous, and in some cases, the solution may not even converge because they should be at least as good as the constrained variant. In this example, the solution was calculated 15 times for each point, and the optimal solution was selected. It should be noted that the solutions are, in many cases, inferior in terms of the reconstruction error to those obtained with constraints. Therefore, it can be concluded that the power constraints do not alter the solution space in a way that results in significantly inferior solutions, but they lead to solutions that are in the vicinity of local minima of the unconstrained solution space. Additionally, it can be observed that the constrained solutions consistently exhibit an error range of 0.3 to 0.4, which is analogous to the two-step decomposition.

It has been demonstrated that the introduction of supplementary constraints on the

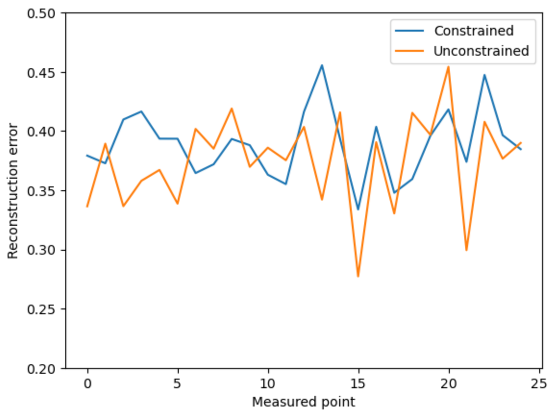

Figure 4.24: The reconstruction error of the decompositions with added constraints and without added constraints for flight 11 (left) and 13 (right).

power of X-Bragg and dihedral results in a unique solution to the cost function, which is also in accordance with the actual measured values. Moreover, the impact of the modifications on the solutions has been examined, and it has been established that several characteristics undergo alteration. For instance, the reconstruction error has been observed to increase. However, it can be assumed that the solutions obtained through the constrained approach are not significantly different from the global optimum of the unconstrained approach. Consequently, the question arises as to how the cost function changes in relation to a few parameters.

4.3.3 Cost function

The objective of this analysis is to examine the cost function in greater detail in order to ascertain the influence of the parameters on it, with a particular focus on the minima and their position. To this end, the cost function is considered as a function of ε_s, as this is the parameter used to calculate the soil moisture. The investigation is conducted under the same constraints as in section 4.3.2, with several values fixed for the parameters under investigation. The corresponding reconstruction error is then examined for all possible values of ε_s. It should be noted once more that, for a given set of parameters, the solution obtained is not the optimal one. Consequently, there may be minor fluctuations in the plots. We commence with the parameter m_s.

Parameter: m_s We now proceed to examine the parameter that is closely associated with the power of the X-Bragg model. Upon examination of Fig. 4.25, four

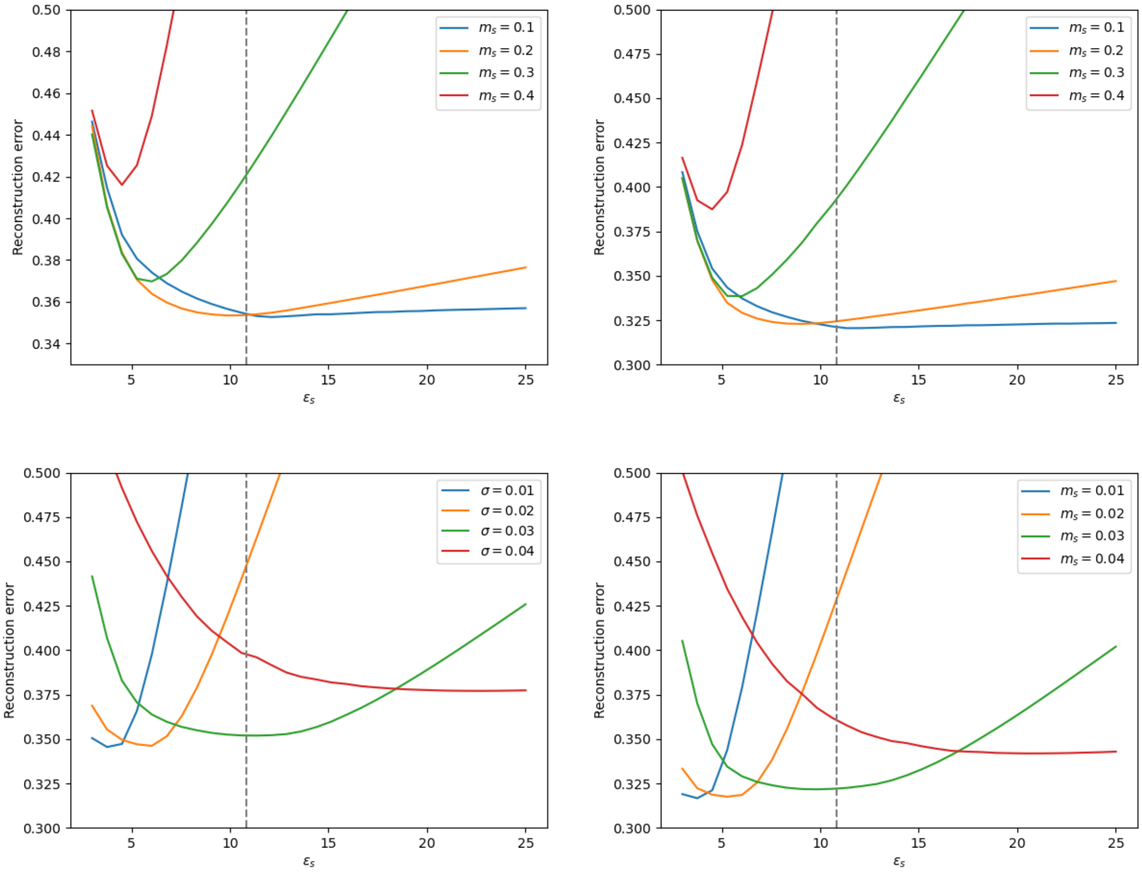

Figure 4.25: The cost functions of two different points depending on ε_s for several m_s (first row) and *sigma* (last row) with the vertical gray line standing for the ground measured value.

distinct functions are observed. It can be discerned that for $m_s = 0.1$ the cost function remains constant from the value $\varepsilon_s = 12$. This would indicate that there is no global optimum, and thus difficulties may be encountered when attempting to calculate a reasonable solution with this constraint. This is due to the fact that the optimisation algorithm could halt at any point within this range, resulting in a different soil moisture value for each new run. As the parameter m_s is increased, the right-hand side of the function gradually becomes more curved upwards, creating a new global minimum. However, this also has the disadvantage of changing the position of the minimum, which has a significant impact on the determination of soil moisture. Depending on the selected value of m_s, different soil moisture values can be forced. However, as can be seen, the soil moisture space that can be influenced is located in the lower half, and higher soil moisture values cannot be forced

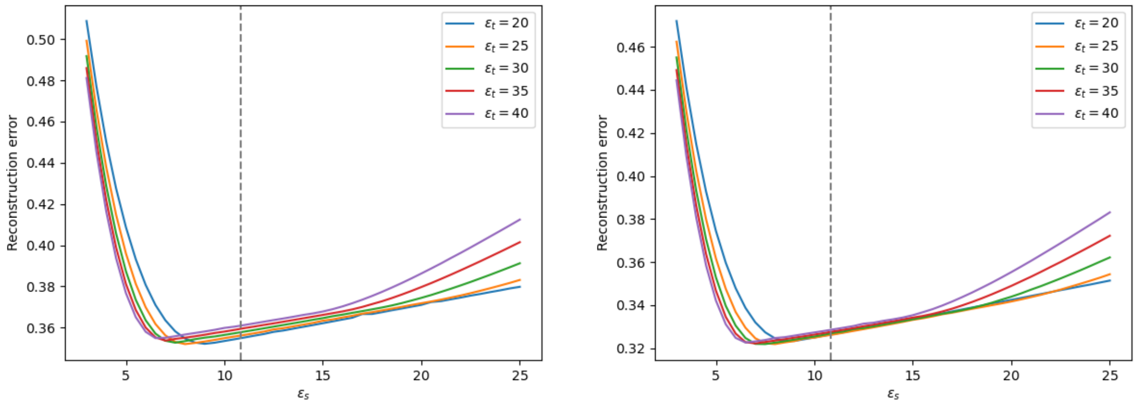

Figure 4.26: The cost functions of two different points depending on ε_s for several ε_t with the vertical gray line standing for the ground measured value.

with the same ease because of the flat cost function in this range, which could be attributed to the decreased X-Bragg sensitivity for high soil moisture values.

Parameter: σ The following section shall examine the influence of the dihedral component. Of particular significance in this context is the parameter Sigma, which represents the deviation of soil roughness. As illustrated in Fig. 4.25, the optimal value shifts towards larger ε_s for elevated σ values, indicating a distinct behavioural pattern. This can be explained by examining the formula for the power and recognising that for larger σ, the power becomes smaller in contrast to m_s in X-Bragg component. However, it is also evident that the choice of constraints can exert a significant influence on the position of the minima and the existence of minima within this range, if we exclude the edges. Similarly, the power parameters appear to exert a significant influence on soil moisture. It would be of interest to ascertain whether the value of ε_t of stem also plays a pivotal role in this context.

Parameter: ε_t The final parameter under consideration is the dielectric constant of the stem, which forms part of the dihedral model. It is notable that the choice of parameter has no discernible impact on the cost function, as illustrated in Fig. 4.26. Despite a possible 4 vol% difference, this has no bearing on the cost function's properties, such as the formation of minima, or on the algorithm's behaviour, including convergence. In conclusion, we shall examine the cost function in the event that the power parameters are permitted to vary freely.

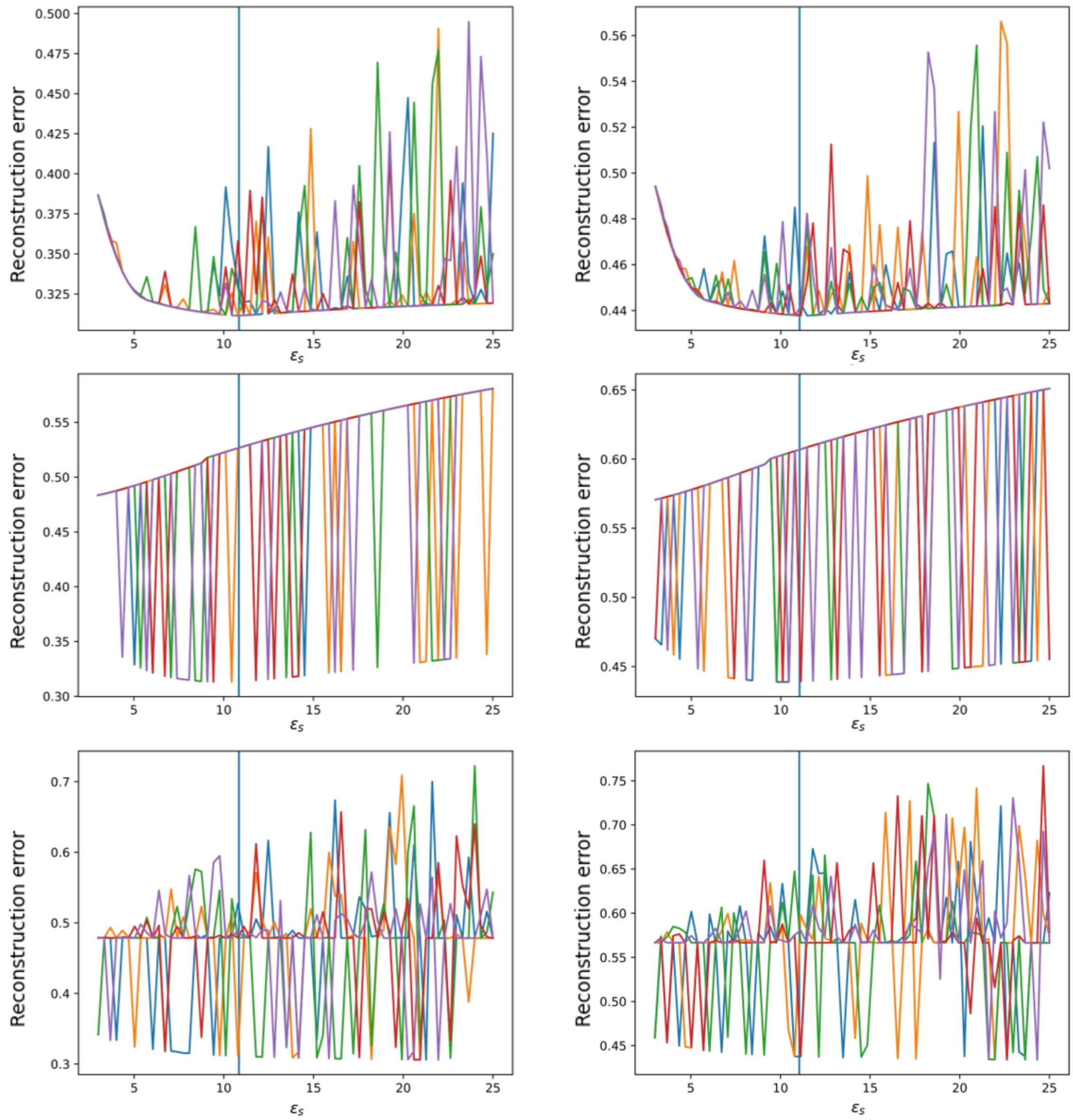

Figure 4.27: The cost functions of two different points depending on ε_s with unconstrained m_s (first row), σ (second row) and both (last row) with 10 different runs.

Convergence and uniqueness As previously demonstrated in section 4.3.1, the majority of parameters fail to converge when the power variable is not subjected to a constraint. Figure 4.27 provides further insight into this phenomenon. In the case where m_s is left unconstrained, the minimum error for small ε_s initially decreases rapidly (in line with the increasing power of the X-Bragg), but then remains constant. When larger ε_s values are considered, it becomes evident that the maximum error increases, and that numerous solutions emerge, which can be

attributed to the algorithm failing to converge or becoming trapped in local minima. This serves to illustrate that the defined cost function, when utilising the specified models, is not sensitive to soil moisture. However, when σ is left unconstrained, two optimas emerge, between which the algorithm makes a transition. Finally, when both parameters are free, the solutions appear to be highly chaotic.
Having previously addressed the one-step decomposition in considerable detail, we have demonstrated the manner in which the physical models can be integrated into the optimisation process of the aforementioned decomposition. We then proceeded to examine the manner in which the introduction of new constraints on the power can be employed to ascertain the soil moisture, and how these constraints impact the cost function and, consequently, the solutions that we calculate. Finally, we turn our attention to the two-step and one-step decomposition, and undertake a comparative analysis of the results.

4.4 Comparison of the one-step and two-step decompositions

4.4.1 Vertical profile of the volume layer

The objective of this section is to examine the discrepancies between the volume polarimetry matrices obtained through the one-step and two-step decomposition processes. To this end, the same area as in Fig. 1 for flights 11 and 13 is examined. As can be observed, there is minimal distinction between the tomograms of flight 11 and the phase centre is situated at an equivalent elevation. However, an evident discrepancy emerges when examining flight 13. The one-step decomposition exhibits more narrow main lobe in comparison to the two-step decomposition, and the phase centre is elevated, suggesting that the signal is more distinct from

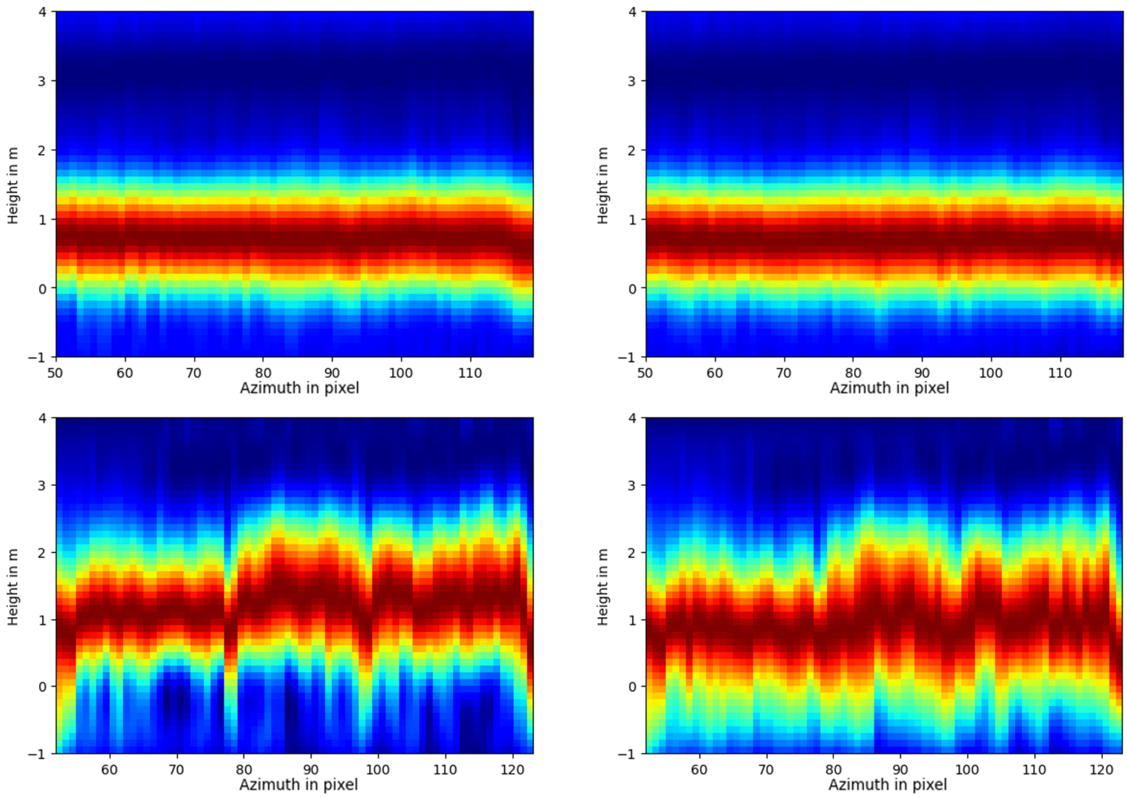

Figure 4.28: Tomograms of the volume structure matrix of the one-step (first column) and two-step (second column) decomposition of the big maize field along the blue line from Fig. 4.4 for flight 11 (first row) and 13 (last row).

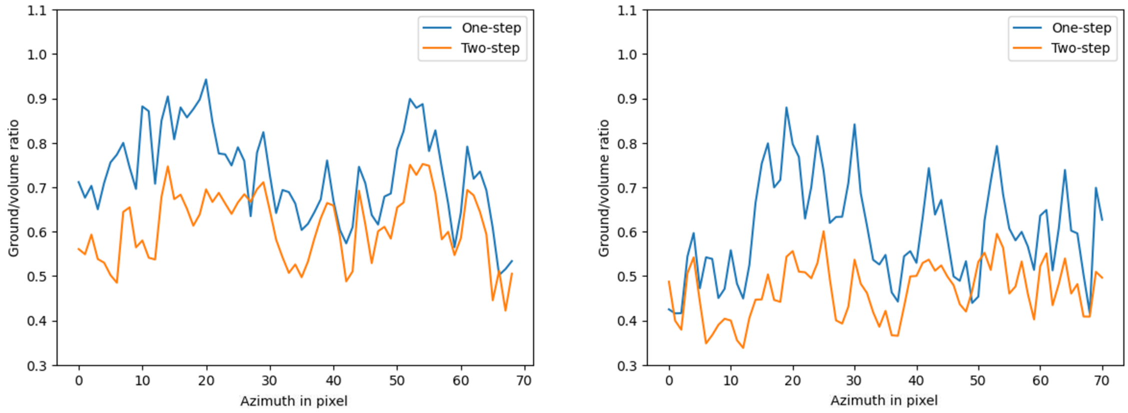

Figure 4.29: Ground-to-volume ratio of the one-step and two-step decomposition for flight 11 (left) and 13 (right).

the ground. One potential explanation for this is that the introduction of physical models for the ground layer facilitates its more effective separation.
Having established that the polarimetry matrices exhibit identical profiles for the two methods under consideration, the objective now is to ascertain whether the powers associated with the ground and volume components are also identical.

4.4.2 Ground-to-volume ratio

A comparison of the ground-to-volume ratios of the two methods (Fig. 4.29) reveals that the one-step decomposition method consistently yields greater relative power for the ground. This is undoubtedly related to the constraints of the one-step decomposition and the integration of physical models. However, an examination of the associated tomograms reveals that the power is distributed more evenly throughout the volume layer of the two step decomposition due to the signal reaching down to the ground. Consequently, a proportion of the volume layer is also present at the height of the ground. It is notable that the ground-to-volume ratios are shifted in relation to one another and exhibit a similar profile. This outcome is to be expected, given the similarities between the two methods.
In light of the preceding discussion on the properties of ground volume separation, it is now pertinent to consider the nature of one-step decomposition in H/α space in comparison to two-step decomposition.

4.4.3 H/α space

The issue with two-step decomposition was that the H/α values from $\mathbf{T}_{ground}$ could not be described using H/α space, as some solutions were situated outside the valid range of X-Bragg and dihedral H/α space. Consequently, the models were incorporated into the optimisation process utilising the one-step method, the outcome of which is illustrated in Fig. 4.30. This figure demonstrates how the preceding results of the two-step decomposition have been drawn into the valid range. It is noteworthy that the values are so proximate in the one-step solution, which is achieved through the utilisation of physical models. The constraints on the powers serve to bring them into closer proximity. Additionally, it is noteworthy to examine the direction in which the novel values are trending. As previously observed in

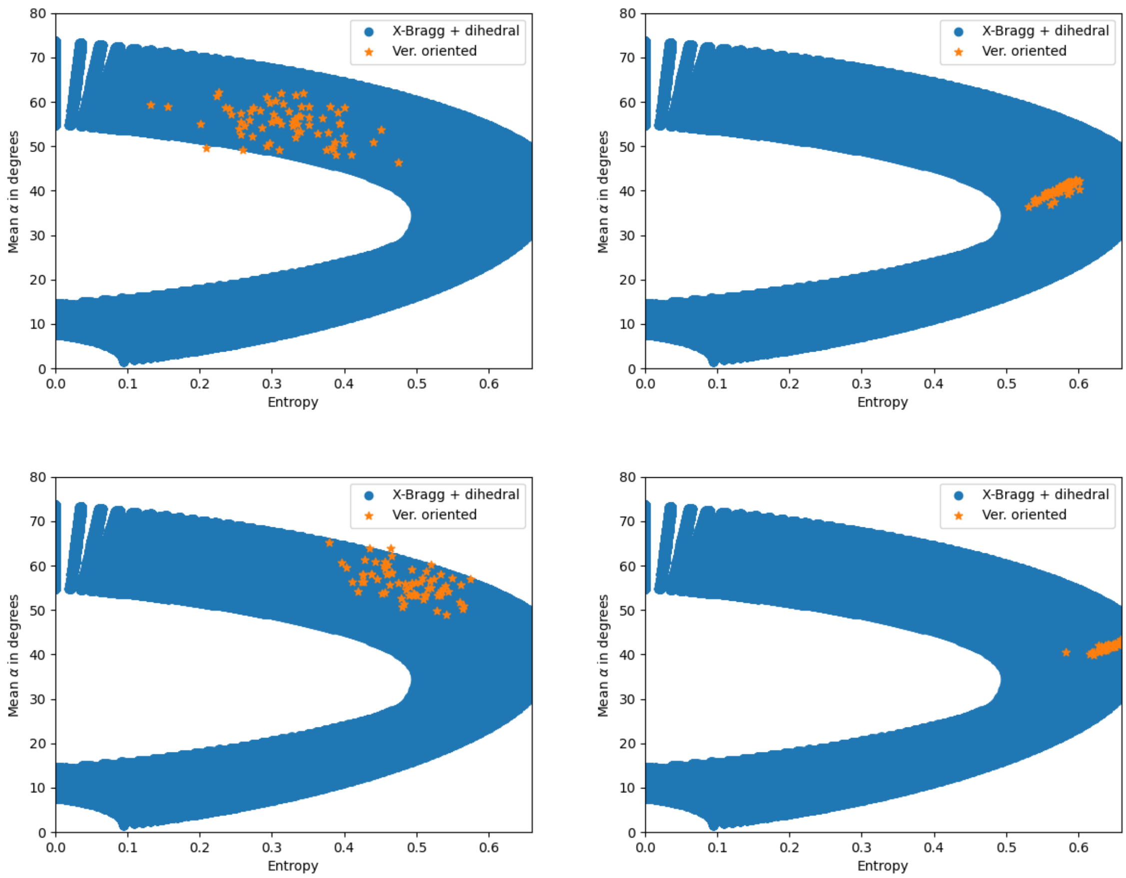

Figure 4.30: H/α space of the resulting $\mathbf{T}_{ground}$ of the two-step (first column) and one-step (second column) decompositions for flight 11 (first row) and 13 (last row).

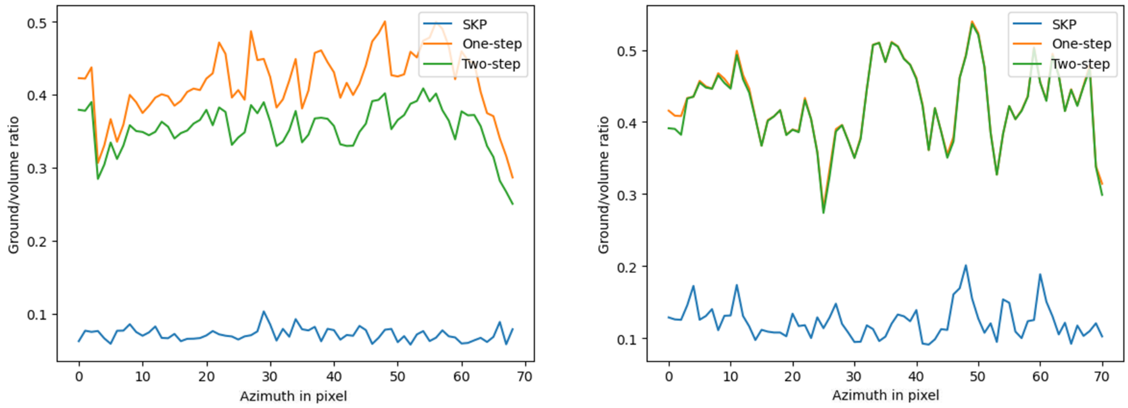

Figure 4.31: The reconstruction error of the one-step and two-step SKP decompositions for flight 11 (left) and 13 (right).

section 4.2.2, there is a tendency to oscillate between distinct phi solutions, with the resulting soil moisture values exhibiting minimal variation.
Finally, an examination of the reconstruction error of the two methods will be undertaken to ascertain the extent to which they are able to describe the data in the same manner.

4.4.4 Reconstruction error

In light of the aforementioned reconstruction error, it can be posited that the two-step decomposition approximates the data more accurately due to the unrestricted nature of $\mathbf{T}_{ground}$, a hypothesis that is corroborated by the data presented in Fig. 4.31. With regard to flight 11, it is evident that the two-step decomposition consistently exhibits a reduced error compared to the one-step decomposition. In the case of flight 13, the errors are found to be approximately equal for the selected points, indicating that the introduction of the physical models does not negatively impact the approximation of the data. When comparing the two methods of the SKP, it becomes evident that there are significant discrepancies in the error, which can be attributed to the fixing of the $\mathbf{R}_{ground}$ to a Dirac signal on height zero and $\mathbf{T}_{volume}$ volume polarimetry matrix. Additionally, it is observed that these restrictions do not yield as accurate a description of the data as when they are absent.

5 Discussion

It would be beneficial to present a few additional considerations that are not included in the results, but which may prove insightful nonetheless. The initial point for discussion is the necessity to define the structure matrix for the ground in the one-step decomposition. One might suggest that it would be sufficient to determine the polarimetry matrix for the ground using the physical models, just as one determines the polarimetry matrix for the vegetation layer. However, this is not an appropriate approach, as the tomograms of the ground structure matrix the scattering center of the X-Bragg scattering contribution is located above the vegetation layer, rather than within the soil. This finding is also consistent with the results obtained from [20]. Therefore, it is essential to set the structure matrix in this instance.
It is also important to consider the reconstruction error, which is used for optimisation to calculate the decomposition and indicates how well the data is approximated. Various constraints have been considered, for example, one variable could be the vertical position for the structure matrix of the grounds portion, while another could be to separate the X-Bragg and dihedral scattering contributions with a separate free structure matrix (to not impose a Dirac signal) for the dihedral component. It is evident that the reduction in the number of constraints results in a decrease in the reconstruction error. This is a logical consequence of the approach taken, with the results approaching those of the standard SKP with no constraints. One might be tempted to conclude that the magnitude of the reconstruction error is negligible, given that all other data can be interpreted as either scatterer or noise, which we seek to filter out in any case. However, it is also important to recognise that an increase in the magnitude of the error is associated with a increased probability of the solutions being rendered ineffectively. This is due to the fact that they may encompass different information, which is not aligned with our desired outcomes. To illustrate this, consider a scenario where a volume component is included, despite the absence of vegetation. In this instance, a portion of the signal is also attributed to this component, which may not be accurate. This naturally gives rise to the ques-

tion of whether the selected cost function (approximation error of the data) is the optimal choice for determining soil moisture, or whether it requires modification.
Another point for consideration is the the choice of the constraints and the corresponding assumptions. It is proposed that the structure matrix for the ground and the polarimetry matrix for the vegetation are fixed. Alternatively, it could be argued that only the structure matrices for the ground and vegetation should be fixed [21]. One advantage of this approach is that it allows for the attainment of unique solutions in the decomposition, which was not the case in our previous analysis when the polarimetry matrix for the ground had full rank.
Furthermore, it has been demonstrated that the accuracy and sensitivity of the physical models observed in H/α space are dependent on the soil moisture content. Specifically, they become less sensitive at higher soil moisture levels. Additionally, when X-Bragg and dihedral are considered together, the power ratio plays a significant role, as evidenced by the findings presented in [22]. Our results reinforce this conclusion, as the acceptable results are only because of the constrained power ratio.

6 Conclusion

The present master's thesis examines the sensitivity of soil moisture estimation using SKP decomposition with additional constraints. This was examined in two ways. The initial approach was the two-step decomposition, whereby the ground and volume were separated in the initial stage. In this approach, the constraints were set such that the first component represents the ground, with the structural matrix assigned to it and the polarimetry matrix of the volume configured to represent the second component, which corresponds to the vegetation layer. Subsequently, we demonstrated that the separation is a viable and effective approach, utilising tomograms to validate the structure matrix of the volume and the H/α space for the polarimetry matrix of the soil. In the second step, we attempted to ascertain the soil moisture from the resulting polarimetry matrix for the ground. We demonstrated that the solutions can be predominantly characterised by the X-Bragg and dihedral model in H/α space. However, the soil moisture determination is not feasible due to ambiguity regarding in the valid range. Nevertheless, we identified the potential for using constraints to resolve this ambiguity.

Consequently, the subsequent phase entailed the incorporation of the physical models into the SKP decomposition, thereby ensuring the generation of results that can be characterised with the X-Bragg and dihedral models and the integration of supplementary constraints for the models. It has been demonstrated that the solution to the model remains ambiguous in the absence of constraints. It was also demonstrated that constraints exist for the determination of appropriate soil moisture. These constraints were then applied to the power of the X-Bragg and dihedral models. The high influence of the power parameters of the models on the estimated soil moisture was also demonstrated with the use of the cost function. Finally, the two methods were compared, and it was observed that the resulting structure matrices for the vegetation were similar, while the solutions for the polarimetry matrix differed. This discrepancy can be attributed to the introduction of constraints that particularly restrict the polarimetry matrix for the ground.

A method for determining soil moisture estimation under vegetation has now been identified as a viable working method. As has been demonstrated, the values are heavily influenced upon the power parameters of the respective physical models to a significant extent, such that a vast range of soil moisture values can be produced, depending on the selected constraints. The challenge now is to determine these constraints in a meaningful way. Additionally, there is the question of the suitability of the cost function for determining soil moisture, as this only specifies the degree of approximation of the data.

Bibliography

[1] Alberto Moreira et al. "A tutorial on synthetic aperture radar". In: *IEEE Geoscience and Remote Sensing Magazine* 1.1 (2013), pp. 6–43. DOI: 10.1109/MGRS.2013.2248301.

[2] I. Hajnsek, E. Pottier, and S.R. Cloude. "Inversion of surface parameters from polarimetric SAR". In: *IEEE Transactions on Geoscience and Remote Sensing* 41.4 (2003), pp. 727–744. DOI: 10.1109/TGRS.2003.810702.

[3] Irena Hajnsek et al. "Potential of Estimating Soil Moisture Under Vegetation Cover by Means of PolSAR". In: *IEEE Transactions on Geoscience and Remote Sensing* 47.2 (2009), pp. 442–454. DOI: 10.1109/TGRS.2008.2009642.

[4] Hannah Joerg et al. "On the Separation of Ground and Volume Scattering Using Multibaseline SAR Data". In: *IEEE Geoscience and Remote Sensing Letters* 14.9 (2017), pp. 1570–1574. DOI: 10.1109/LGRS.2017.2723980.

[5] Stefano Tebaldini. "Algebraic Synthesis of Forest Scenarios From Multibaseline PolInSAR Data". In: *IEEE Transactions on Geoscience and Remote Sensing* 47.12 (2009), pp. 4132–4142. DOI: 10.1109/TGRS.2009.2023785.

[6] Yves Chauvin and David E. Rumelhart. *Backpropagation: Theory, Architectures, and Applications*. Psychology Press, 1995.

[7] Nikita Basargin, Alberto Alonso-González, and Irena Hajnsek. "Constrained Tensor Decompositions for SAR Data: Agricultural Polarimetric Time Series Analysis". In: *IEEE Transactions on Geoscience and Remote Sensing* 61 (2023), pp. 1–13. DOI: 10.1109/TGRS.2023.3331599.

[8] S. Cloude. *Polarisation: Applications in Remote Sensing*. OUP Oxford, 2010. ISBN: 9780199569731. URL: https://books.google.de/books?id=krAVDAAAQBAJ.

[9] Africa Flores et al. *The SAR Handbook: Comprehensive Methodologies for Forest Monitoring and Biomass Estimation*. Apr. 2019. DOI: 10.25966/nr2c-s697.

[10] Gilbert Strang. *Linear Algebra and Its Applications*. 3rd. Academic Press, 1993.

[11] A. Freeman and S.L. Durden. "A three-component scattering model for polarimetric SAR data". In: *IEEE Transactions on Geoscience and Remote Sensing* 36.3 (1998), pp. 963–973. DOI: 10.1109/36.673687.

[12] Gianfranco Fornaro and Vito Pascazio. "Chapter 20 - SAR Interferometry and Tomography: Theory and Applications". In: *Academic Press Library in Signal Processing: Volume 2*. Ed. by Nicholas D. Sidiropoulos et al. Vol. 2. Academic Press Library in Signal Processing. Elsevier, 2014, pp. 1043–1117. DOI: https://doi.org/10.1016/B978-0-12-396500-4.00020-X. URL: https://www.sciencedirect.com/science/article/pii/B978012396500400020X.

[13] Jorge Nocedal and Stephen J Wright. *Numerical Optimization*. Springer, 2006.

[14] Diederik P. Kingma and Jimmy Ba. *Adam: A Method for Stochastic Optimization*. 2017. arXiv: 1412.6980 [cs.LG]. URL: https://arxiv.org/abs/1412.6980.

[15] Ralf Horn et al. "F-SAR — DLR's new multifrequency polarimetric airborne SAR". In: *2009 IEEE International Geoscience and Remote Sensing Symposium*. Vol. 2. 2009, pp. II-902-II–905. DOI: 10.1109/IGARSS.2009.5418244.

[16] Mario Lezcano-Casado. *Trivializations for Gradient-Based Optimization on Manifolds*. 2019. arXiv: 1909.09501 [cs.LG]. URL: https://arxiv.org/abs/1909.09501.

[17] Kefeng Ji and Yonghui Wu. "Scattering Mechanism Extraction by a Modified Cloude-Pottier Decomposition for Dual Polarization SAR". In: *Remote Sensing* 7 (June 2015), pp. 7447–7470. DOI: 10.3390/rs70607447.

[18] George Clarke Topp, J. les Davis, and A. Peter Annan. "Electromagnetic determination of soil water content: Measurements in coaxial transmission lines". In: *Water Resources Research* 16 (1980), pp. 574–582. URL: https://api.semanticscholar.org/CorpusID:128732424.

[19] Fawwaz T. Ulaby and R. P. Jedlicka. "Microwave Dielectric Properties of Plant Materials". In: *IEEE Transactions on Geoscience and Remote Sensing* GE-22.4 (1984), pp. 406–415. DOI: 10.1109/TGRS.1984.350644.

[20] J. David Ballester-Berman and Juan M. Lopez-Sanchez. "Applying the Freeman–Durden Decomposition Concept to Polarimetric SAR Interferometry". In: *IEEE Transactions on Geoscience and Remote Sensing* 48.1 (2010), pp. 466–479. DOI: 10.1109/TGRS.2009.2024304.

[21] Alberto Alonso-González, Emanuel Hecht, and Kostas Papathanassiou. “Polinsar Two Layer Model Ground and Volume Respone Separation”. In: *IGARSS 2019 - 2019 IEEE International Geoscience and Remote Sensing Symposium*. 2019, pp. 4931–4934. DOI: 10.1109/IGARSS.2019.8900629.

[22] Hannah Joerg et al. “Investigating Soil Moisture Dependency of the Ground Polarimetry under Agricultural Vegetation Estimated by SAR Tomography”. In: *EUSAR 2018; 12th European Conference on Synthetic Aperture Radar*. 2018, pp. 1–5.

List of Figures

List of Tables